Journal Pre-proof

Novel WC-reinforced iron-based composites with excellent mechanical properties synthesized by laser additive manufacturing: underlying role of reinforcement weight fraction

Hongyu Chen (Data curation) (Investigation) (Methodology) (Visualization) (Writing - original draft), Dongdong Gu (Conceptualization) (Methodology)<ce:contributor-role>Supervision, Validation) (Writing - review and editing), Hongmei Zhang (Data curation) (Investigation), Lixia Xi (Validation), Tiwen Lu (Data curation) (Investigation), Liang Deng (Data curation) (Investigation), Uta Kühn (Supervision), Konrad Kosiba (Validation) (Visualization) (Writing - review and editing)

PII: S0924-0136(20)30376-9

DOI: https://doi.org/10.1016/j.jmatprotec.2020.116959

Reference: PROTEC 116959

To appear in: *Journal of Materials Processing Tech.*

Received Date: 9 June 2020

Revised Date: 19 October 2020

Accepted Date: 26 October 2020

Please cite this article as: Chen H, Gu D, Zhang H, Xi L, Lu T, Deng L, Kühn U, Kosiba K, Novel WC-reinforced iron-based composites with excellent mechanical properties synthesized by laser additive manufacturing: underlying role of reinforcement weight fraction, *Journal of Materials Processing Tech.* (2020), doi: https://doi.org/10.1016/j.jmatprotec.2020.116959

This is a PDF file of an article that has undergone enhancements after acceptance, such as the addition of a cover page and metadata, and formatting for readability, but it is not yet the definitive version of record. This version will undergo additional copyediting, typesetting and review before it is published in its final form, but we are providing this version to give early visibility of the article. Please note that, during the production process, errors may be discovered which could affect the content, and all legal disclaimers that apply to the journal pertain.

© 2020 Published by Elsevier.

Journal Pre-proof

Novel WC-reinforced iron-based composites with excellent mechanical properties synthesized by laser additive manufacturing: underlying role of reinforcement weight fraction

Hongyu Chen[1,2], Dongdong Gu[1,2,*]dongdonggu@nuaa.edu.cn, Hongmei Zhang[1,2], Lixia Xi[1,2],Tiwen Lu[3], Liang Deng[3], Uta Kühn[3], Konrad Kosiba[3]

[1] College of Materials Science and Technology, Nanjing University of Aeronautics and Astronautics (NUAA), Yudao Street 29, Nanjing 210016, Jiangsu Province, PR China

[2] Jiangsu Provincial Engineering Laboratory for Laser Additive Manufacturing of High-Performance Metallic Components, Nanjing University of Aeronautics and Astronautics, Yudao Street 29, Nanjing 210016, Jiangsu Province, PR China

[3] Leibniz IFW Dresden, Institute for Complex Materials, P.O. Box 27 01 16, D-01171 Dresden, Germany

*Corresponding author. Tel./fax: +86 25 52112626;

(D. Gu).

Abstract

Laser powder bed fusion (LPBF) process was utilized to prepare high-performance steel matrix composites (SMCs) consisting of a tool steel (1.2767L) matrix with various contents of submicron-sized WC reinforcing particles. The influence of the content of WC reinforcing particles on constitutional phase, microstructural evolution, densification rate and mechanical properties of SMCs was investigated. It shows that the microstructures and mechanical properties of SMC are highly sensitive to the WC-content. A higher weight fraction of WC leads to a reduced martensite start temperature (M_s) since more W and C atoms are dissolved within the iron matrix during the LPBF-process. The microstructure consists of more retained austenite using a higher WC-content. The addition of 2 wt% WC particles enables a significant grain refinement of the iron-based

Journal Pre-proof

matrix, due to the formation of a $(Fe,W)_6C$ carbidic network that restricts the growth of the sub-grain boundaries of the parent austenite. This refinement-effect is less pronounced at higher WC content due to the reduced self-diffusion activation energy of the Fe atoms in the parent austenite. Increasing WC-content also increases the thickness of the carbidic network, leading to a reduced directionality in the texture of the composite-microstructure. Compared with the unreinforced steel parts, the composites reinforced with 2 wt% WC show a synergetic reinforcing effect in compressive strength of ~3210 MPa and fracture strain up to ~30.2% and ultimate tensile strength of ~1677 MPa and elongation of ~8.5%. The improved mechanical properties result from the combined effect of transformation-induced plasticity (TRIP) effect, grain refinement, non-equilibrium grain-boundary strengthening, and nano-scaled precipitation.

Keyword: Additive manufacturing; Laser powder bed fusion; Steel matrix composite; Microstructure; Mechanical property

1. Introduction

The significance of strengthening steels with ceramic particles, which leads to steel matrix composites (SMCs), has been widely acknowledged in modern industries. SMCs are generally fabricated via casting or powder metallurgy methods and the major challenge in synthesizing high-performance SMCs by these preparation techniques is to homogenize the microstructure with the uniformly distributed reinforcing particles, as revealed by Chawla (2019). Almangour et al. (2018) demonstrated that, because of large attractive van der Waals forces effective between the small-sized reinforcing particulates, the dispersed distribution of reinforcing particles within metal matrix is very challenging. Gu et al. (2020) also reported that the rapid growth of the reinforcing phases is a further challenge. Fortunately, these challenges can be overcome by applying laser powder bed

Journal Pre-proof

fusion (LPBF) technology as a processing route. Pauly et al. (2018) demonstrated that LPBF is a workable laser additive manufacturing (LAM) technology capable of fabricating SMCs not only with complex shape, but also with designed and tailored microstructures. Kalentics et al. (2019) also illuminated that LPBF is a promising tool for tailoring metallic microstructures and resulting mechanical by applying appropriate processing parameters and post-treatment method. LPBF enables the manufacturing of multi-functional and high-performance SMCs-components, significantly expanding its applicability.

In recent years, LPBF has been successfully employed to the fabrication of SMCs with superior mechanical properties, benefiting from its unique solidification behavior. Boegelein et al. (2015) reported that selective laser melted oxide dispersion strengthened (ODS) ferritic steels show a large improvement in physical and mechanical properties, deriving from the fine dispersion of nanoscopic Y(Al, Ti) oxides in the steel matrix. However, their microstructure reveals an intense [001] texture along the building direction, thus exhibiting a strong anisotropy in Young's modulus and yield strength. Almangour et al. (2018) added micro- and nano-TiC particles into 316L stainless steel and prepared the SMCs by LPBF. They demonstrated that the incorporation of TiC particles to the steel powder considerably decreases the cellular and grain sizes in solidified microstructure and also disrupted the inherent directional texture feature. The TiC-reinforced SMCs, therefore, exhibit higher room- and high-temperature mechanical properties than unreinforced steel. Li et al. (2019) prepared vanadium carbide reinforced 316L stainless SMCs using LPBF and they found that the room-temperature tensile

Journal Pre-proof

strength of the as-fabricated 316L matrix composites is much higher than that of as-fabricated 316L stainless steel. The ultrafast non-equilibrium melting/solidification nature of LPBF enables the particulates to distribute uniformly along the boundaries of austenite grains, thus inhibiting against the growth of austenite matrix and contributing to the strengthening effect of the fabricated SMCs. Besides oxide-, TiC- and VC-reinforced SMCs, a material class that strongly benefits from the unique solidification feature of LPBF is the WC particles reinforced SMCs. Their excellent properties result from the following mechanisms: (i) W diffusion into the iron-based matrix leading to effective solution strengthening, as revealed by Yan et al. (2019); (ii) Song et al. (2020) demonstrated that C atoms act as a strong austenite former and thus achieve the formation of austenite/martensite matrix showing improved strength and ductility owing to the transformation-induced plasticity (TRIP) effect; (iii) Zhang et al. (2019) proposed that small-sized WC particles act as heterogeneous nucleants for the primary equilibrium phases during solidification of the molten pool by providing low-energy-barrier nucleation sites at the solid/liquid interface. However, great advantages often involve great challenges, which is particularly pronounced for the high tendency of cracking during LPBF-synthesized WC-reinforced SMCs. Gu et al. (2018) have optimized the processing parameters for fabricating high-densification-level WC-steel composites by LPBF. However, owing to the uncontrollable formation of brittle compounds during LPBF, a fragile reaction layer between partially melted WC particles and Fe-based matrix forms and usually acts as crack initiation site. Liu et al. (2008) also reported similar results. With the increasing WC content, more crack initiation sites appeared within the

Journal Pre-proof

composites, which was detrimental for their mechanical properties, as demonstrated by Wang et al. (2016). As a consequence, the optimization of the WC content is pivotal for the preparation of high-performance SMCs.

In the present study, the submicron-sized (<1 μm) WC particles, used as reinforcing phase, were mixed with 1.2767L tool steel powder to produce high-performance SMCs via LPBF. Chen et al. (2020) have demonstrated that submicron-sized WC particles can be completely melted during LPBF, leading to the formation of novel in-situ nanoscale reinforcements within the substructure of SMCs instead of brittle compounds formed at the interface between WC particles and Fe-based matrix. Therefore, the processing defects such as the formation of cracking or non-uniform microstructures can be avoided and the high-performance WC/Fe composites can be synthesized successfully. The focus of this study is to synthesize tool steels containing 0, 2, 4 and 6 wt% submicron-sized WC reinforcing particles and, accordingly, characterize and compare their microstructures and mechanical properties. Since the 1.2767L tool steel is widely used in mould industry including forging and pressing tools, stamping tools, bending tools, highly stressed coining tools, and plastic molds, a high impact resistance combined with high compressive strength is required to meet its application demands, as demonstrated by Chen et al. (2017). The compressive properties of SMCs reinforced with different weight fraction of WC were tested in this study and the corresponding fracture mechanisms were revealed. Since the tensile property is another key performance indicator for additive manufactured solid parts, the tensile testing for SMCs samples were also conducted in this study. Thus, the strength-ductility relations of the SMCs prepared via LPBF can be

Journal Pre-proof

further revealed. Our work discloses the interrelation between the fraction of reinforcement, resulting microstructure and mechanical properties of the SMC samples. The SMCs components with a unique combination of strengthening mechanisms and improved performance are successfully fabricated. We believe that LBPF possesses a promising method to prepare low-cost SMCs components meeting the increasing requirements for higher performance in the future industrial applications.

2. Experimental method

2.1 Powder preparation

Spherical gas-atomized 1.2767L tool steel powder with a mean particle size of 21.6 µm (Fig. 1a and b) and spherical WC powder with a mean size of around 600 nm were processed in this work. Three different WC/steel composite systems containing 2 wt%, 4 wt% and 6 wt% WC particles (further named SMC-2WC, SMC-4WC, and SMC-6WC) were produced using low energy ball milling method in a Pulverisette 6 planetary mono-mill (Fritsch GmbH, Germany). The ball-to-powder weight was 2:1. The milling time was 4h and the rotation speed was set at 200 rpm, using argon atmosphere to prevent the composite powder from oxidation. The as-prepared composite powders are shown in Figs. 1c-h, in which the WC particles are the high contrast materials (gray color) on the surface of the steel powder. The size and morphology of the steel powder were not altered during low energy ball milling in comparison to the pure iron-based powder. Consequently, the composite powders also provide a nice flowability, as revealed by Gu et al. (2019).

Journal Pre-proof

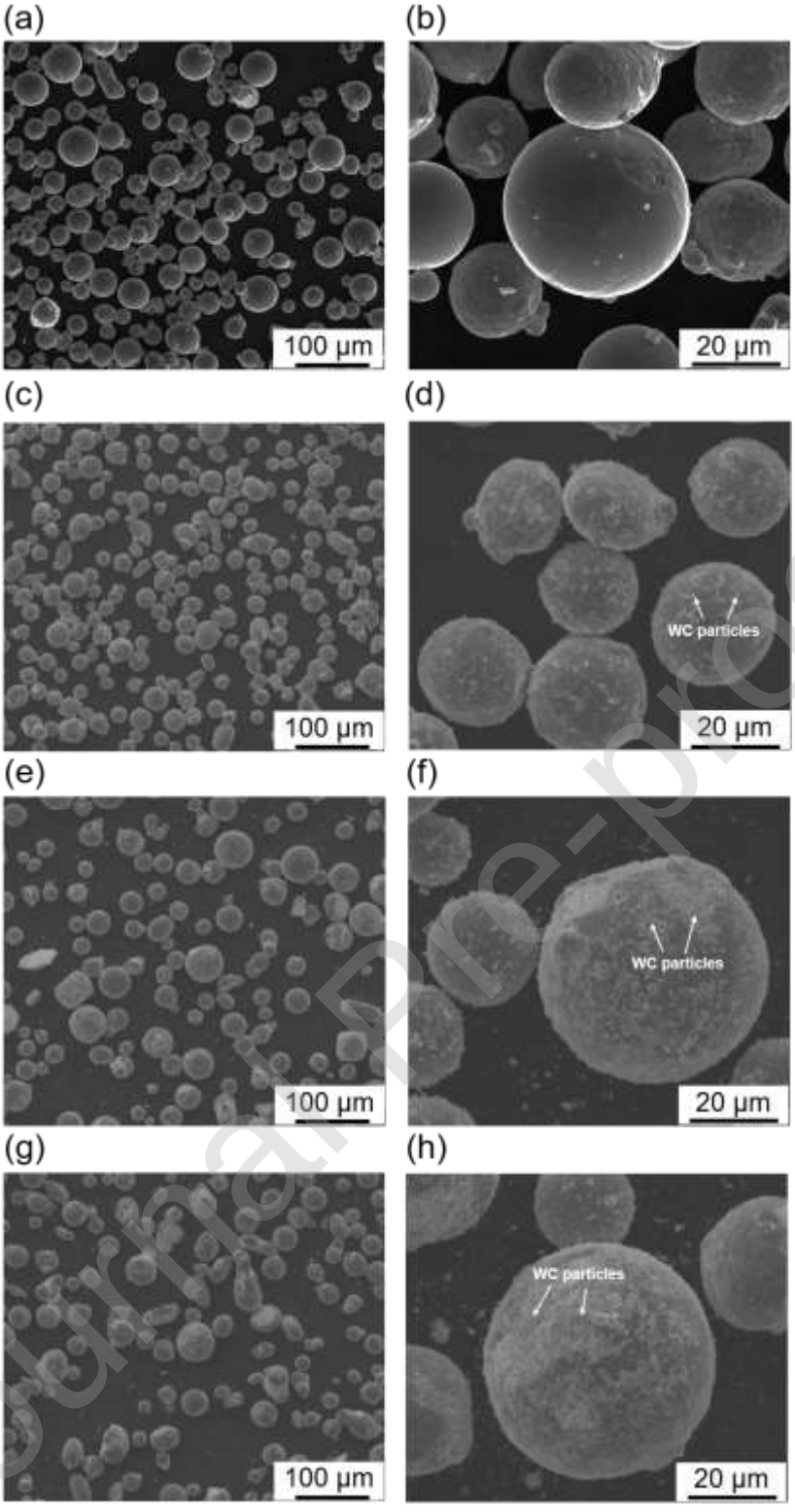

Fig. 1 Scanning electron microscope (SEM) images show typical morphologies of the tool steel powder (a) and as-prepared composite powder containing different weight fraction of WC particles: (c)-(d) 2 wt% WC; (e)-(f) 4 wt% WC; (g)-(h) 6 wt% WC.

Journal Pre-proof

2.2 Laser powder bed fusion process

The LPBF process was performed using a NUAA self-developed LPBF-150 device. The detailed processing procedures have been given in Gu et al. (2018) work. Based on our previous experiments, an optimized processing parameter was set to obtain high-density LPBF-fabricated samples as follows: laser power P = 450 W, laser scanning speed v = 1500 mm/s, layer thickness h = 30 μm and hatching space s = 50 μm. A checker scan mode was used to reduce the evolution of thermal stress during LPBF processing. Each layer was divided into numerous small square islands (5 mm × 5 mm) and the laser melted these islands in the designated sequence. The process was repeated until the bulk parts (10 mm × 10 mm× 5 mm) were produced for microstructural characterization. cylindrical samples (⌀3 mm, length 6 mm) were fabricated in the building direction for compression tests and tensile specimens (according to ASTM E8 standard) were prepared in the horizontal direction with respect to the building direction for tensile tests.

2.3 Microstructural characterization

The relative densities of the LPBF-fabricated specimens were measured by computed X-ray tomography (μ-CT, phoenix nanotom m, GE) and the distribution of metallurgical defects within LPBF-fabricated samples was determined by μ-CT reconstruction. X-ray diffraction (XRD; STOE Stadi P, Co $K_{\alpha 1}$ radiation) was conducted on polished samples to identify the phases constitution in the LPBF-fabricated composite material. The microstructure was characterized by a field emission scanning electron microscope (SEM; Leo 1530 Gemini) also enabling energy-dispersive X-ray spectroscopy (EDS; Quantax400 with SDD-Detector Xflash4010, Bruker) spot analyses

Journal Pre-proof

to determine the chemical composition of the LPBF-manufactured composites, as demonstrated by Gao et al. (2020). Phase distribution, micro-texture, grain size and grain boundary distribution were analyzed by electron backscattered diffraction (EBSD) in a NANO SEM 430 (FEI, Hillsboro, Oregon). Inverse pole figures (IPF) maps and pole figures (PF) at the upper surface of the LPBF-fabricated bulk sample were attained from three different orientations (BD, TD and ND). Thereby, BD corresponds to the building direction, TD to the transverse direction parallel to the upper surface of the substrate, and ND is the normal direction with respect to the lateral surface, which is vertical to the surface of the substrate of the sample. The scanning step size for the IPF map was set to 0.1 μm.

2.4 Mechanical testing

A MTS Landmark 370 (MTS Systems Corporation, USA) was used to perform quasi-static compression tests on the SMC samples at room temperature. In order to alleviate the frictional effect, the upper and bottom surfaces of all compression samples were lubricated with zinc stearate prior to compression testing. The displacement rate was 0.1 mm/min. At least three specimens were tested to ensure the reproductivity of the data. The fracture surfaces were also observed by SEM (Leo 1530 Gemini SEM at 20 kV). A MTS 810 (MTS Systems Corporation, USA) was used to conduct tensile tests at room temperature. An extensometer with ceramic extension rods contacted with the gauge section of the tensile specimens directly and the axial strain can be recorded. The strain rate was set at $5 \times 10^{-4} s^{-1}$.

3. Results and discussion

Journal Pre-proof

3.1 Densification behavior

Fig. 2 illustrates the μ-CT reconstruction maps and corresponding relative density (RD) of the LPBF-fabricated steel and SMC samples reinforced with different WC content. The relative densities of the LPBF-fabricated samples show a linear decrease from 99.8% (LPBF-fabricated 1.2767L steel, Fig. 2a) to 97.4% as the WC content increases to 6 wt% (Fig. 2d). This demonstrates that fully dense SMCs parts are difficult to be realized with increasing WC particle concentration in the Fe-based powder. The main metallurgical defects within LPBF-fabricated SMCs are cracks with horizontal propagation directions and irregular pores (Fig. 2b, c and d). Wang et al. (2016) have demonstrated that, since the thermal expansion coefficients of steel are much higher than that of WC, an increase of WC content can augment the difference in thermal expansion coefficients between composites and matrix. Consequently, a larger thermal stress was obtained in the SMCs reinforced with higher WC content and thus it is inclined to cause cracking within the SMCs samples. Additionally, the homogeneity of WC particles in the composite powder also poses great influence on the processing quality of SMCs. From Fig. 1f and h, there are still un-mixed WC particles (satellite particles) observed around the mixed powder with 4 and 6 wt% WC particles added. By contrast, all the submicron-sized WC particles are uniformly dispersed on the surface of the steel powder particles with 2 wt% WC particles added (Fig. 1b). This indicates that, more WC particles added to the steel powder, more difficult to achieve the uniform distribution of WC particles in the composite powder. The limited homogeneity of WC particles restricts the fabrication of fully dense SMCs. Thus, in the SMC-4WC and SMC-6WC samples, more irregular

Journal Pre-proof

pores can be observed compared to the SMC-2WC samples.

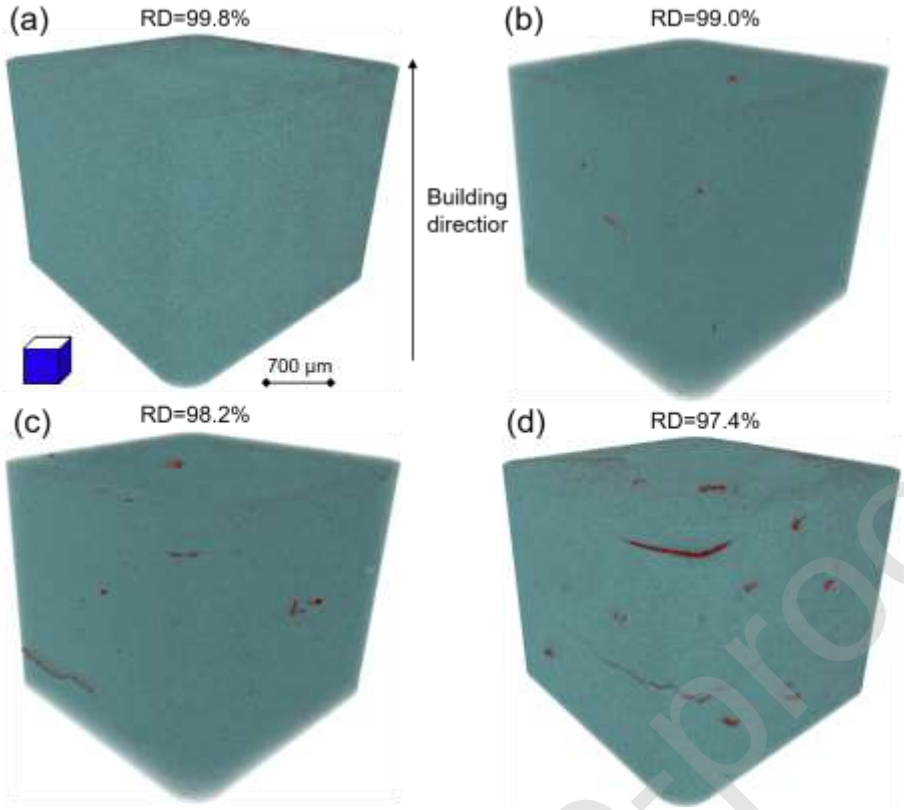

Fig. 2 The µ-CTs reveal the distribution of pores within LPBF-fabricated 1.2767L tool steel (a) and composite samples reinforced with (b) 2 wt% WC, (c) 4 wt% WC and (d) 6 wt% WC.

3.2 Phase analysis

Fig. 3 shows the typical XRD patterns of the LPBF-fabricated steel and SMC samples reinforced with different weight fractions of WC particles (2, 4 and 6 wt%). Strong diffractions corresponding to martensite were observed in all representative samples, so that martensite was the dominant phase within the microstructure. An increasing content of WC particles changed the constitutional phase of the iron-based matrix, as can be seen from the evolution of the ratio of the peak intensities between martensite and austenite. Fig. 4 displays the distribution of martensite and austenite within the iron-based matrix by means of an EBSD analysis. With increasing WC-content, also

Journal Pre-proof

the fraction of austenite increased, but the phase distribution within the iron-based matrix was very different. The SMC-2WC shows a uniform distribution of austenite with a relatively low volume fraction of 10.3%. As the content of WC increased to 4 wt%, the austenite was strongly clustered and its volume fraction increased to 15.4%. Further increasing the content of WC to 6 wt% entailed a dramatical increase of retained austenite (39.9 vol.%). Diffraction corresponding to WC cannot be observed in the XRD patterns of SMC-2WC and SMC-4WC, indicating that the WC particles should undergo a complete dissolution within the iron-based matrix during the LPBF process. This is in line with Chen et al. (2020)'s study. By contrast, diffraction peaks appendant to the $(Fe,W)_6C$ carbide were present for the iron-based composite reinforced with 6 wt% WC. The Fe-based matrix is supersaturated and not capable, anymore, to incorporate more W and C atoms directly into the iron-based solid solution during this strong non-equilibrium-processing at ultrahigh cooling rates. As a consequence, excessive W and C elements precipitate as additional carbidic phase.

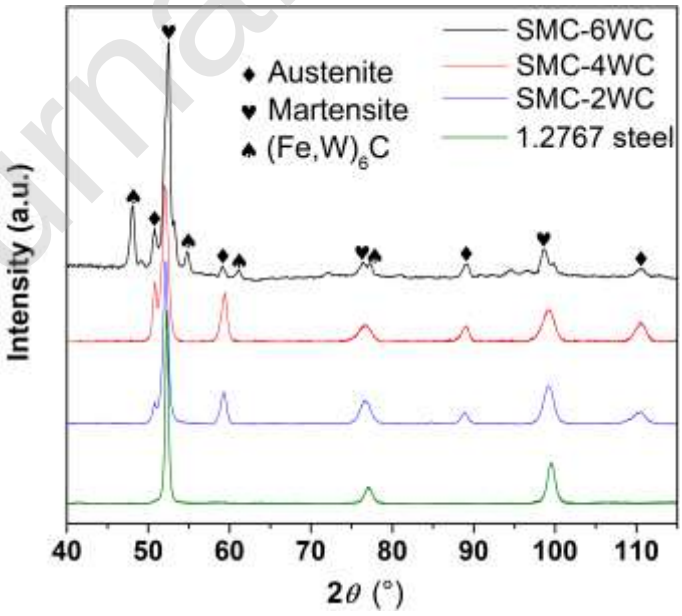

Fig. 3 XRD patterns of LPBF-fabricated tool steel and composite samples reinforced with

Journal Pre-proof

different content of WC.

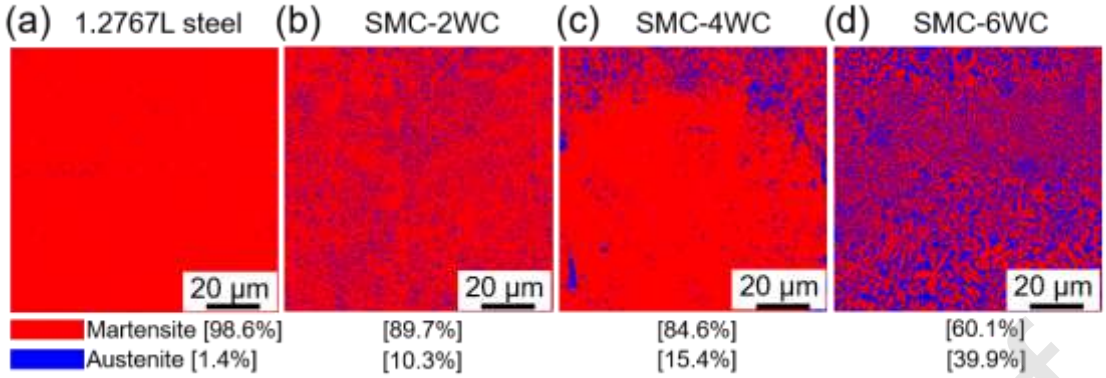

Fig. 4 EBSD analysis shows the phase map and volume fraction of austenite and martensite within LPBF-fabricated 1.2767L tool steel (a) and composite samples reinforced with (b) 2 wt% WC, (c) 4 wt% WC and (d) 6 wt% WC.

During LPBF-processing tool steel materials, a large amount of solidified austenite transforms into martensite owing to the self-quenching effect, as reported by Sander et al. (2016). Chen et al. (2018) also revealed that a complete lath martensite microstructure can be obtained in the LPBF-fabricated tool steel owing to the substantially large cooling rate during the solidification of molten pool. However, the martensitic structure in heat affected zone (HAZ) would retransform into austenite during the SLM processing of the next powder layer. The austenite then will again transform into martensite due to the following self-quenching effect. Nevertheless, a small amount of austenite is retained within the final solidified parts, since the temperature of molten pool cannot reach the martensite finish temperature (M_f) because of the constant thermal cycling effect during SLM. This phenomenon was also revealed by Holzweissig et al. (2015). Thus, a mixed martensitic/austenitic microstructure can be obtained, as shown in Fig. 4a. With the

Journal Pre-proof

incorporation of WC particles, the W and C elements dissolve within the iron-based matrix during LPBF processing and significantly affect the phase transformation of iron between austenite and martensite. Borm et al. (2006) proposed that it can be characterized by the Gibbs-Thomson capillarity effect which in the present case to describe the solubility of WC particle in the Fe-based melt:

$$\frac{RT\rho}{M}\ln\frac{S_1}{S_2}=2\sigma\left(\frac{1}{r_1}-\frac{1}{r_2}\right), \quad (1)$$

where M is the molecular weight of WC particle in the Fe-based solvent, T is the absolute temperature, ρ is the density of WC, σ is the interfacial tension between WC particle and Fe-based liquid, S_1 and S_2 are the solubilities of WC particles with radius r_1 and r_2 ($r_1>r_2$) and R is the gas constant. Eq. (1) implies that the WC particles will be completely dissolved within the iron-based matrix, if the size of WC particles is extremely small (submicron-sized). This is in line with the results obtained from the XRD analysis confirming that no diffraction corresponding to WC carbides are visible. Both W and C elements can reduce the martensite start temperature (M_s) and, hence, increase the volume fraction of the retained austenite within the iron-based matrix, as revealed by van Bohemen (2012). Compared to the unreinforced steel samples, the volume fraction of retained austenite in SMC-2WC shows a large increase to 10.3% (Fig. 4b). As the content of WC increases up to 4 wt%, more W and C elements dissolve within the iron-based matrix, further decreasing the M_s even below the room temperature. Thus, a large amount of austenite does not transform back to martensite after the temperature within the HAZ goes below room temperature, which causes the retained austenite to aggregate within the

Journal Pre-proof

HAZ in the final solidified microstructure, as shown in Fig. 4c and d. As expected, a further increase of the WC-content up to 6 wt% causes more retained austenite. We can infer that large numbers of diffused W and C solubilizes within the iron-based matrix as substitutional and interstitial atoms and affect the phase transformation between austenite and martensite. Additionally, diffused C atoms also contribute to the formation of the carbide-type M_6C with the carbide forming elements, such as Fe and W, according to the XRD pattern of the SMC-6WC sample. One can argue for SMC-2WC and SMC-4WC, the volume fraction of the carbidic phase is below the resolution limit of the XRD device used, but still present. As we will show in the following, the M_6C type carbide also forms in the LPBF-fabricated SMC-2WC and SMC-4WC, but to a lesser extent.

3.3 Microstructural characterization

Fig 5a displays a representative SEM microstructural image of the unreinforced tool steel sample prepared by LPBF, whereas Fig. 5b, c and d depict the microstructures of LPBF-fabricated SMC-2WC, SMC-4WC and SMC-6WC samples. Typical martensite laths were observed in the microstructure of the unreinforced steel, which is in line with the XRD results. With adding 2 wt% WC, the microstructure changes to a cellular structure with the presence of ring-like shaped secondary phases with an average thickness of 120 nm which precipitated along the cell boundaries. The lath-like martensitic structure was observed underneath the precipitated ring-like phases since the martensite was etched out prior to the SEM testing. As the content of WC increased to 4 wt% and further to 6 wt%, the mean thickness of the precipitated phases rose to 145 nm and further to 178 nm, respectively. Figs. 5e-g display the EDS spectrums corresponding

Journal Pre-proof

to the locations indicated with red crosses in Figs. 5b-d. Based on the XRD and EDS analysis, one can determine the ring-like phases to be $(Fe,W)_6C$ type carbide, which is in line with Gu et al. (2018)'s study. With the addition of 2 wt% and 4 wt% WC, these carbides were not identified by XRD because of their low volume fraction. The EDS spectrums demonstrate that the carbidic phase is enriched in W with increasing WC reinforcing content, while it is increasingly depleted in Fe. Consequently, the atomic ratio of Fe and W elements within the $(Fe,W)_6C$ carbide varies for the iron-based composites reinforced with different fractions of WC.

Journal Pre-proof

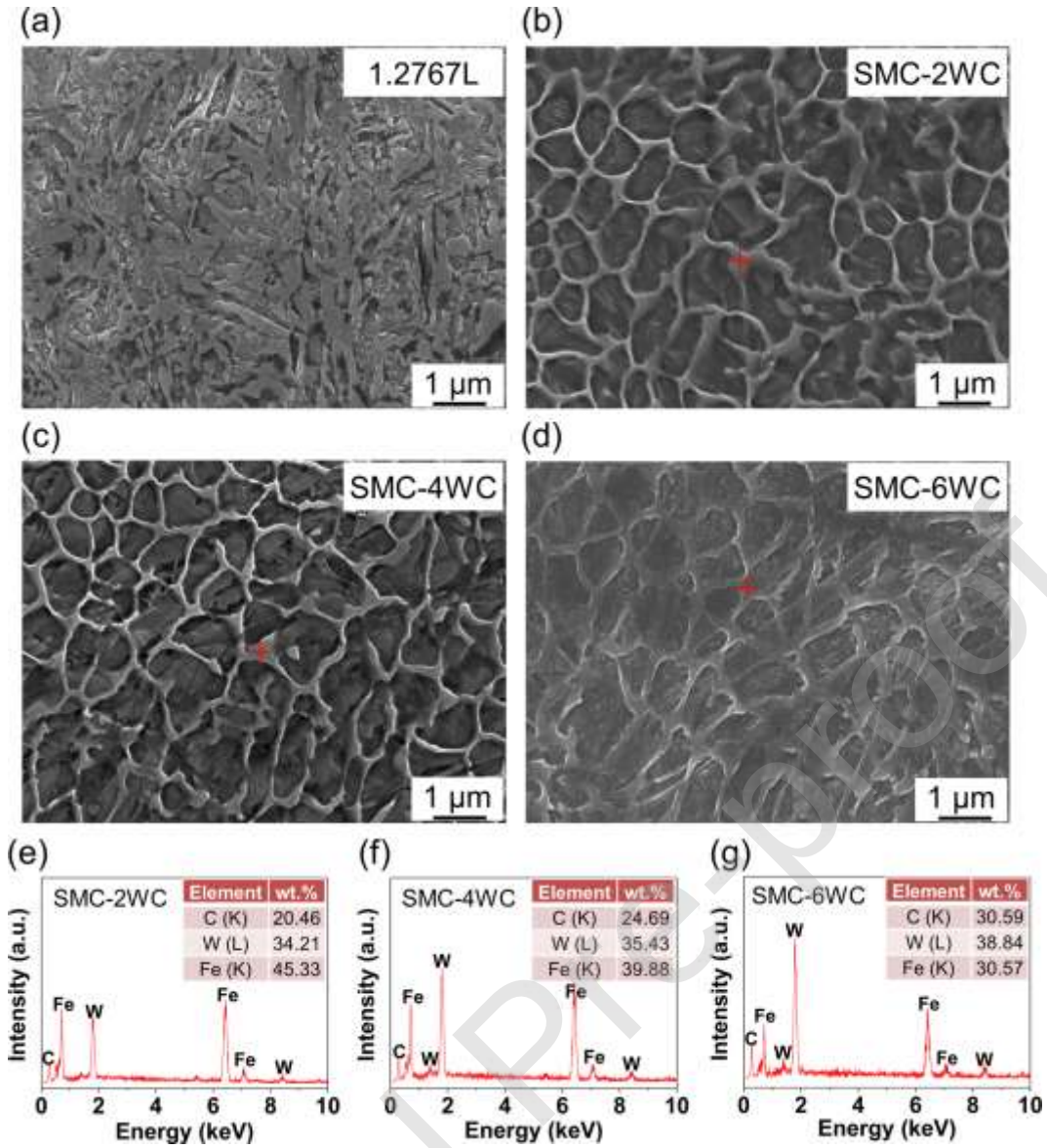

Fig. 5 SEM images highlight the martensite microstructure of 1.2767L tool steel (a) and cellular microstructure of the composite reinforced with (b) 2 wt% WC, (c) 4 wt% WC and (d) 6 wt% WC. (e)-(f) depict the respective EDS analysis carried out at the locations indicated with the red crosses in (b)-(d).

Figs. 6 and 7 show EBSD orientation maps and the corresponding grain size distribution of the iron-based matrices with different additions of WC. At all composite microstructures, lath-martensite structures can be clearly observed and the size of the martensite laths distinctly differs dependent on the weight fraction of WC. The

Journal Pre-proof

unreinforced steel sample revealed relatively large martensite blocks with an average size of 2.79 μm. With addition of 2 wt% WC, these martensite laths became much shorter and narrower with an average size of 0.59 μm. The introduction of WC hence induces a significant grain refinement effect of the Fe-based matrix. At samples processed with 4 wt% WC, the martensite laths became coarser again (average size = 1.10 μm) when compared to the SMC-2WC. With further addition of WC up to 6 wt%, there was no further remarkable change of the martensite lath size. Instead, a higher isotropic feature of the iron-based matrix was obtained, as can be seen from the continuous change of color in the orientation map, e.g. the red/blue/green regions.

Journal Pre-proof

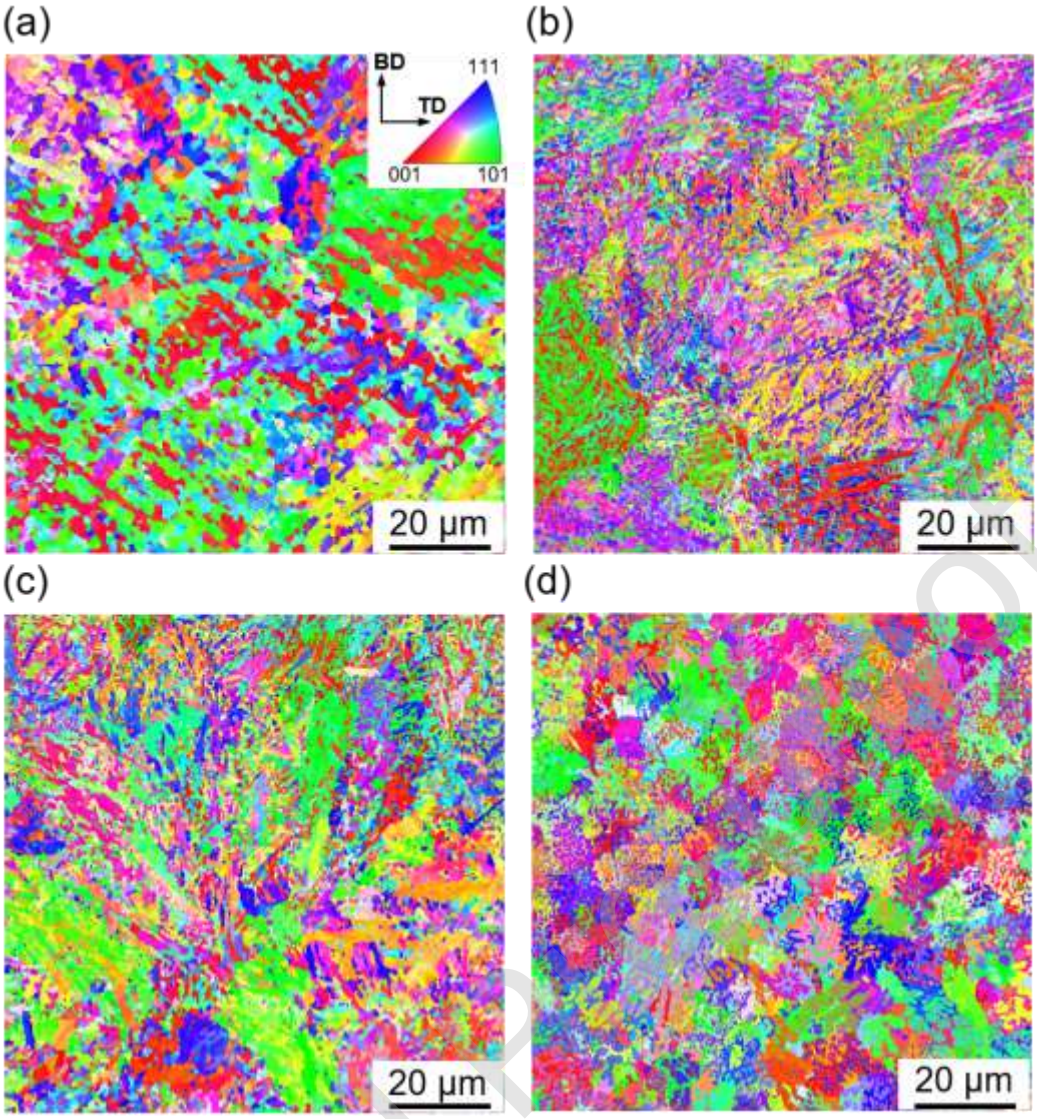

Fig. 6 Inverse Pole Figure (IPF) mapping of LPBF-fabricated 1.2767L tool steel (a) and iron-based matrix within composite samples reinforced with (b) 2 wt% WC, (c) 4 wt% WC and (d) 6 wt% WC.

Journal Pre-proof

Journal Pre-proof

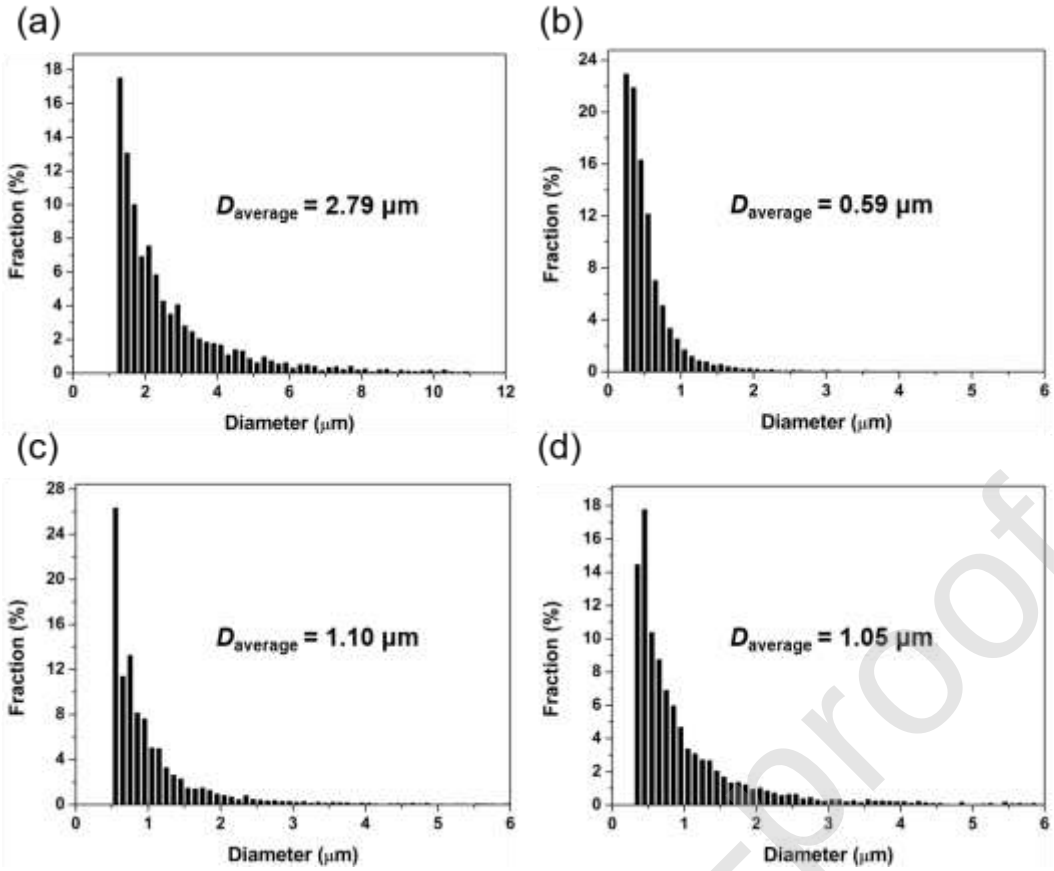

Fig. 7 EBSD analysis shows the grain size distribution for LPBF-fabricated 1.2767L tool steel (a) and iron-based matrix in composite samples reinforced with (b) 2 wt% WC, (c) 4 wt% WC and (d) 6 wt% WC.

The cellular ring-like grains are typical microstructural feature of LPBF-processed iron-based alloys, as demonstrated by AlMangour et al. (2016). During the rapid non-equilibrium solidification process, W and C segregates along the cell boundaries and favors the precipitation of $(Fe, W)_6C$ carbide. AlMangour et al. (2019) believed that these cells are generally not considered as true grains, but sub-grains of the parent austenite. Due to the large cooling rate during LPBF, kinetic constraints are effective on the phase evolution. The alloying elements do not have enough time to segregate to the grain boundary, and instead, they diffuse to the sub-grain boundaries, ultimately leading to the

Journal Pre-proof

formation of the $(Fe,W)_6C$ carbidic phase along the cell boundaries. Li et al. (2019) reported that the disperse distribution of ultrafine carbides along sub-grain boundaries can substantially contribute to the inhibition against austenite growth resulting from the deposition of subsequent layers. Thus, the martensite is much more refined in the composite with the addition of 2 wt% WC compared to the unreinforced iron-based samples. With increasing WC content up to 4 and 6 wt%, more C atoms segregate at the sub-grain boundaries of the parent austenite. According to Vasilyev et al. (2011), the self-diffusion activation energy of the Fe atom in austenite is reduced when the C content at the sub-grain boundaries increases. Typically, the transformation kinetics of the austenite crystal structure, such as grain growth, recrystallization, and the austenite-martensite transformation, is controlled to a significant extent by the rate of the diffusion transfer of Fe atoms through the intergrain/interphase boundary, as reported by Bokshteyn (1961). The decreased self-diffusion activation energy of the Fe atoms facilitates the formation and migration of vacancies, and hence, leads to the formation of coarser austenite grains. Consequently, coarser martensite laths would form along different habit planes in a parent austenite. However, the SMC-6WC samples exhibit a strong isotropic microstructure (Fig. 6). Thus, one can infer that the increase of the $(Fe, W)_6C$ carbide fraction greatly affect the crystal misorientation of grains of LPBF-processed composites and we will dwell on this aspect in the following.

3.4 Grain misorientation analysis

Based on the misorientation angles of grains, three different types of boundaries were identified and they are illustrated in Fig. 8: (I) 2° to 15° (red) corresponding to low-

Journal Pre-proof

angle grain boundaries (LAGBs), (II) 15° to 66.8° (black) corresponding to high-angle grain boundaries (HAGBs) and (III) phase boundaries (blue). It can be found that the martensite laths were separated by HAGBs (>15°, black color) and, additionally, LAGBs (<15°, red color) were visible within the laths, which serve as sub-grain boundaries formed via dislocation rearrangements, as revealed by AlMangour et al. (2017). The proportion of LAGBs and HAGBs within martensite and austenite differs for the composites reinforced with different WC contents. Fig. 9 depicts the misorientation angle distribution for martensite and austenite in LPBF-fabricated iron-based composites reinforced with different content of WC. At the unreinforced steel sample, the fraction of LAGBs and HAGBs within the martensitic microstructure is near to 1:1, while the austenite grains were almost separated by LAGBs (97.6%). With increasing WC content to 2 and 4 wt%, the proportion of LAGBs in martensite and austenite shows a decreased trend to ~40% and ~80%, respectively. Further increasing the fraction of WC to 6 wt% increases the fraction of HAGBs in both martensite (80.8%) and austenite (91.8%). So that, the HAGBs pose the main grain boundary type for the microstructure of the iron-based composite reinforced with 6 wt% WC. The different proportion of HAGBs and LAGBs in austenite and martensite generally leads to different crystallographic micro-texture of LPBF-fabricated samples. Pole figures (PFs) were determined for each composite and Fig. 10 depicts the PF plots quantifying the intensities of texture along the <001>, <101> and <111> crystallographic orientations of martensitic phases with respect to the upper surface of the fabricated sample. Since martensite constitutes the main phase of the composite-microstructure, only the PF plots of martensite were given. A clear trend

Journal Pre-proof

can be observed: the overall crystallographic micro-texture of the martensite gradually decreases (the exp. intensity$_{max}$ decreases from 4.2 to 2.0) with an increasing WC content. This indicates that a higher fraction of WC reinforcement significantly leads to more isotropic microstructure of the LPBF-manufactured composites.

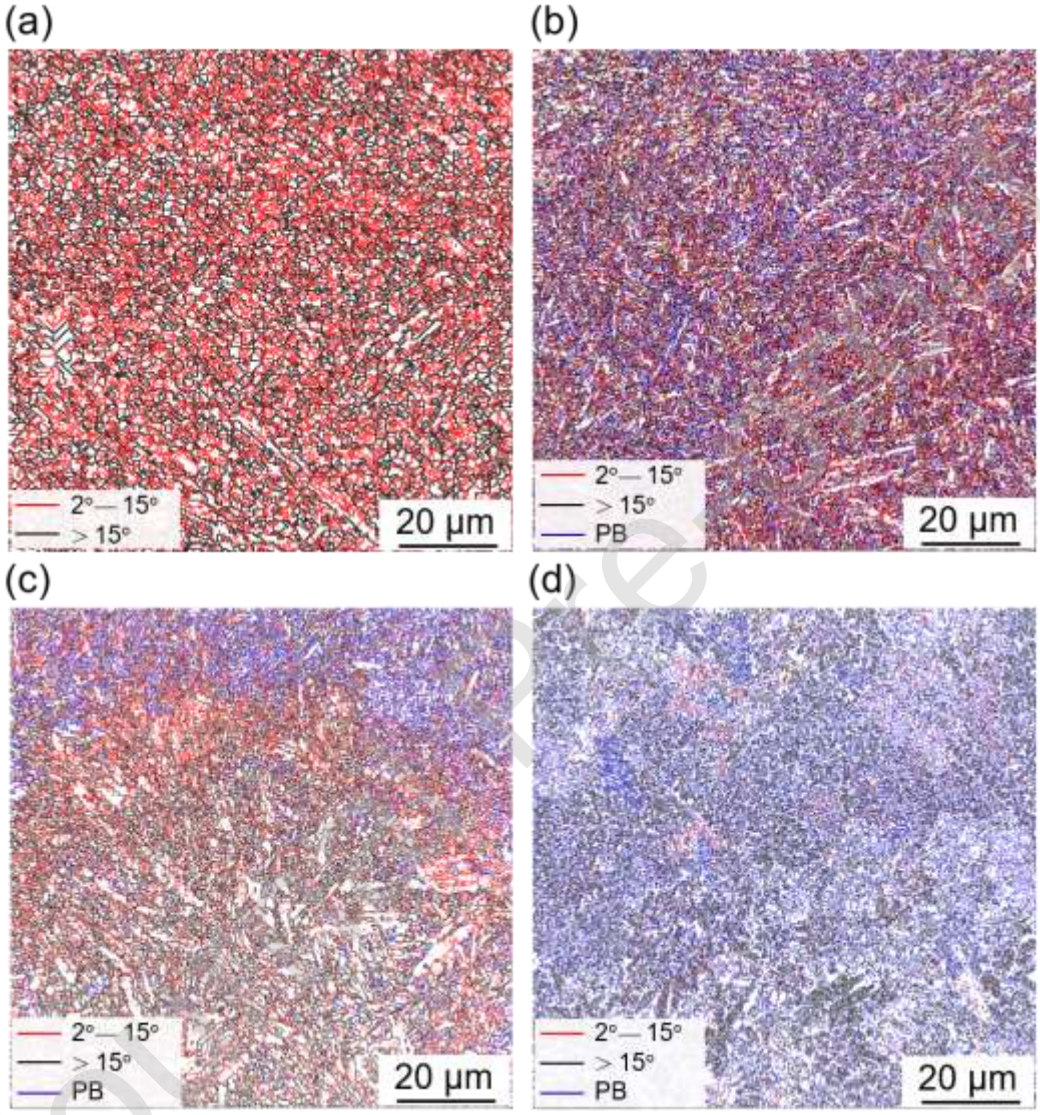

Fig. 8 Grain boundary distribution map for LPBF-fabricated 1.2767L tool steel (a) and iron-based matrix in composite samples reinforced with (b) 2 wt% WC, (c) 4 wt% WC and (d) 6 wt% WC. Thereby, HAGBs are defined with a misorientation angle of 15°-66.8° and LAGBs are defined with a misorientation angle of 2°-15°.

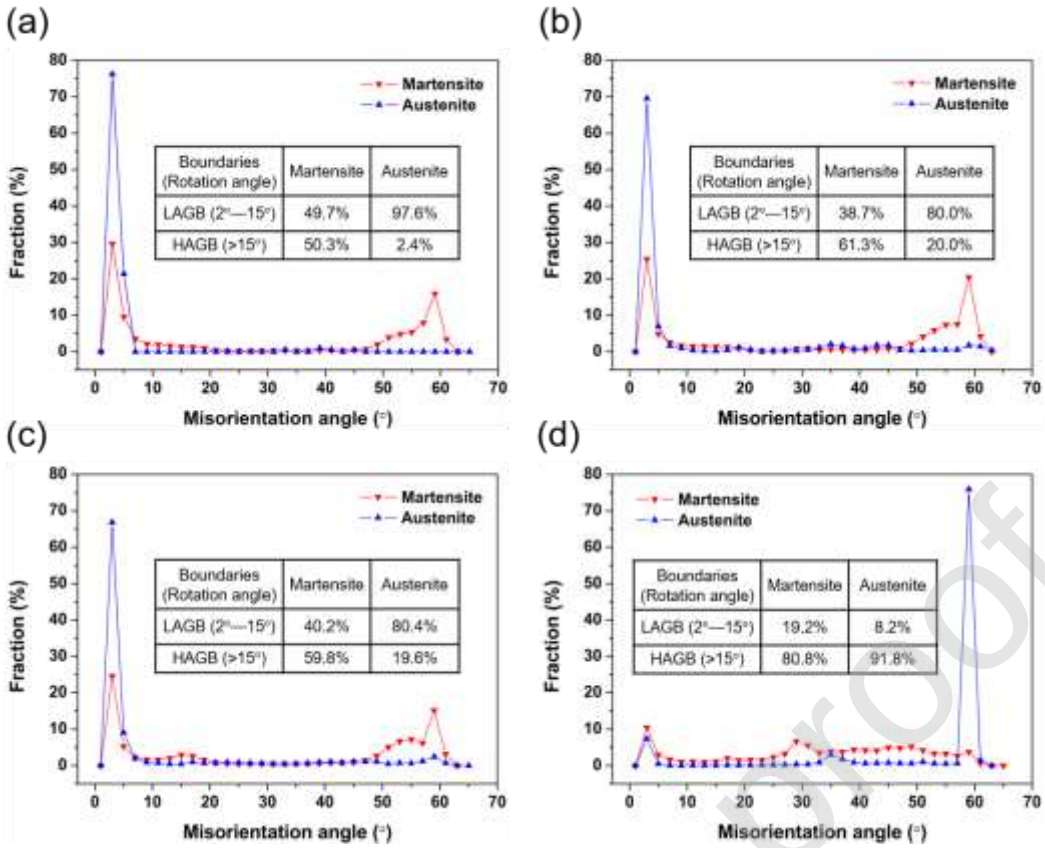

Fig. 9 Misorientation angle distribution for martensite and austenite in LPBF-fabricated 1.2767L tool steel (a) and composite samples reinforced with (b) 2 wt% WC, (c) 4 wt% WC and (d) 6 wt% WC.

Journal Pre-proof

Journal Pre-proof

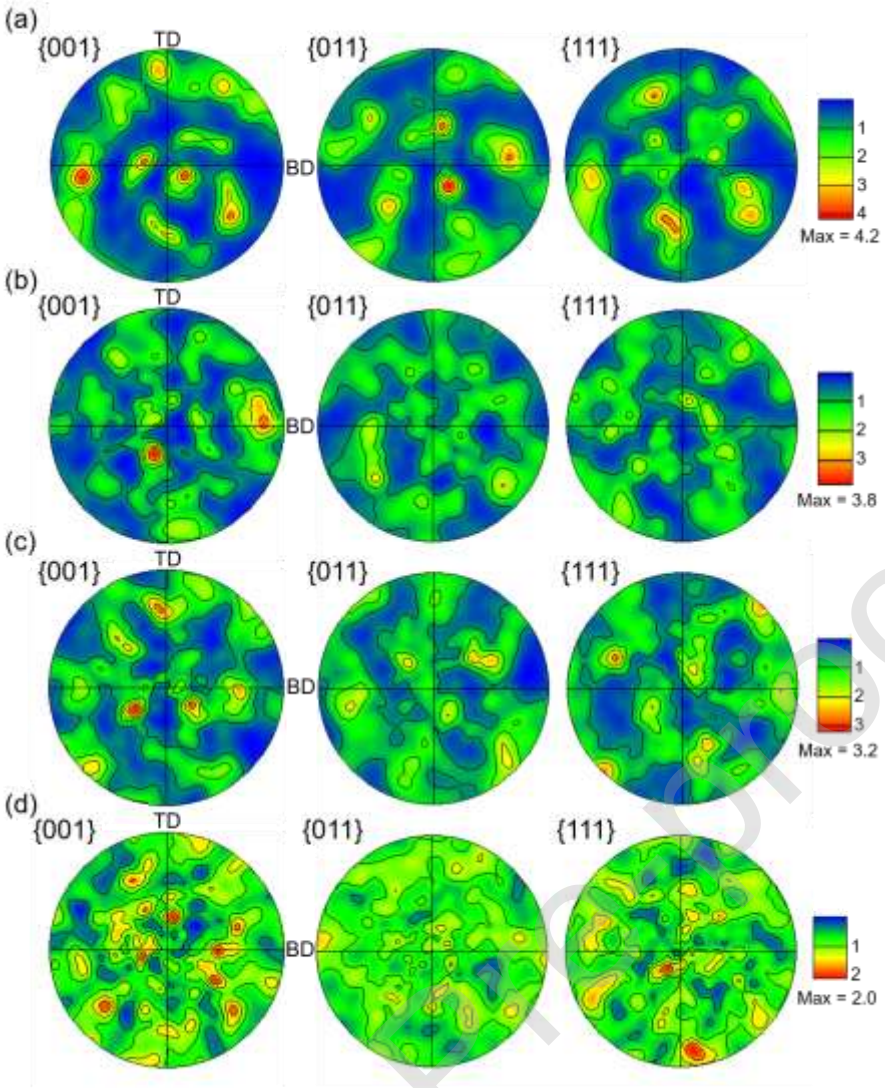

Fig. 10 Pole figure (PF) plots quantify the intensities of texture along the <001>, <101> and <111> crystallographic orientations of martensitic phases with respect to the upper surface of the LPBF-fabricated 1.2767L tool steel (a) and composite samples reinforced with (b) 2 wt% WC, (c) 4 wt% WC and (d) 6 wt% WC.

The microstructure of LPBF-fabricated material always entails substantial internal boundaries, chemical segregations and sub-grain structures due to local lattice distortions and microsegregation effects, as suggested by Wang et al. (2018). Thereby, the unreinforced iron-based samples contain a large number of LAGBs, because of the prevailing formation of lath martensite which is always accompanied by a high density

Journal Pre-proof

of dislocations. With increasing WC content, the fraction of (Fe, W)$_6$C type carbide increases and, as already in the previous section discussed, this carbidic phase generally forms along the sub-grain boundaries of the parent austenite. The (Fe,W)$_6$C carbide can significantly affect the crystal orientation of the martensite. Hirotsu and Nagakura (1972) reported that, in the vicinity of carbide, the martensite laths are always oriented with respect to one of the adjacent lattices of the carbide according to a certain orientation relationship. Thus, the presence of (Fe, W)$_6$C carbides entails a highly random dispersion of martensitic grains and the carbidic precipitations separate these grains via large misorientation angles. This effect is also valid for the retained austenitic grains, since they result from the retransformation of martensite. The misorientation angle distribution in the SMC-6WC samples further demonstrates the effect of (Fe,W)$_6$C carbides on the crystal orientation of martensite. In this condition, most grains keep a large misorientation angle with each other and the composite material shows a strong isotropic microstructure, which is beneficial for an isotropy in mechanical properties.

3.5 Mechanical properties

The engineering compressive stress-strain curves of LPBF-fabricated SMCs reinforced with different WC content are depicted in Fig. 11. Fig. 12 gives the morphologies of the fracture surface of the corresponding samples and so the underlying fracture mechanisms can be revealed. The unreinforced steel samples show a relatively low compression strength of 2722 ± 101 MPa and limited fracture strain of 24.3 ± 1.8%. The attendant fracture surface (Figs. 12a and b) shows a morphology typical of ductile failure mechanism. One can observe a deep dimple-like structure indicative of a ductile

Journal Pre-proof

fracture as is known of unreinforced steels. With the addition of WC up to 2 wt%, the composites show a synergetic improvement in compression strength and fracture strain to 3210 ± 131 MPa and 30.2 ± 2.3%, respectively. As is known from Pacchioni (2017), the ceramic-particle reinforcing mechanism leads to the improvement of strength at the expense of ductility. This relation is called strength-ductility trade-off dilemma, which is not valid for the composite fabricated in this work. According to Liu et al. (2013), the strength and ductility for metal matrix composites can be simultaneously improved via (1) grain refinement, (2) non-equilibrium grain boundaries, and (3) precipitation of nano-scaled particles. The synthesized SMCs show a considerably refined microstructure compared to the unreinforced steel samples, which entails a simultaneous improvement in strength and ductility. According to the well-known theory of non-equilibrium grain boundaries proposed by Su et al. (2020), an increase in the LAGBs augments the density of movable dislocations at the grain boundaries, facilitating dislocation slip and, ultimately, plastic deformation. Furthermore, Zhang and Chen (2006) proposed that a fine dispersion of reinforcing particulates within the metal matrix, like the $(Fe, W)_6C$ carbides with a network-like structure, can effectively hinder the movement of dislocations during deformation, thus further strengthening the composite material. Additionally, as revealed by Song et al. (2020), for steel materials, the transformation-induced plasticity (TRIP) effect provided by the retained austenite in the SMCs is competent in improving the strength and ductility of steel simultaneously. In order to verify the TRIP effect during the compression test, the phase constituent of SMCs after compression tests were measured and the results are given in Fig. 13. It can be found that after the compression test, only

Journal Pre-proof

5.2 vol.% retained austenite can be detected in the SMC-2WC samples based on the calculation of the XRD pattern. This means that majority of retained austenite transforms to martensite during deformation, which can increase work-hardening rate and contribute transformation strain to total elongation. Deformation features resulting from these mechanisms can be observed at the respective fracture surface, as revealed by Fig. 12c. A mixture of a smooth shear and rough zone is visible. The flat zones reveal slip bands and the rough zones show dramatically refined dimples arising from the obtained ultra-fined grains (Fig. 12d). The SMC-4WC showed a further increase of compression strength to ~3485 ± 164 MPa, whereas, the fracture strain decreases to 25.6 ± 2.7%. This demonstrates that the formation of a thicker $(Fe, W)_6C$ carbidic network strengthens the composite material but is detrimental to its plastic deformability. The TRIP effect also occurs in the SMC-4WC samples based on the analysis of the XRD patterns of the fractured samples in Fig. 13, which determines the content of retained austenite in the sample to be 6.7 vol.% after the compression test. The corresponding fracture surface (Figs. 12e and f) shows a high similarity to the one of the SMC-2WC samples, indicating a similar fracture mechanism during compressive loading. With further increasing WC content to 6 wt%, the compressive properties of LPBF-fabricated composite deteriorate, as demonstrated by a reduced compression strength of about ~3051 ± 186 MPa and fracture strain of about 16.2 ± 2.1%. Multiple fracture zones initiated by several apparent cracks can be observed on the respective fracture surface (Figs. 12g and h). The decreased ductility is due to the increase in the number of metallurgical defects within the samples and larger brittleness arising from the increased fraction of $(Fe,W)_6C$ carbides as well as

Journal Pre-proof

high concentration of C in the martensitic matrix. As a consequence, the fracture surface shows a typical brittle fracture mode. The content of retained austenite in the fractured SMC-6WC samples was detected to be 35.5 vol.%, which is close to the value before the compression test (39.9 vol.%). This demonstrates that the TRIP effect in SMC-6WC samples is much less pronounced during the compression test compared to that in the SMC-2WC and SMC-4WC samples. Zhang et al. (2019) demonstrated that the martensite transformation rate is dependent on the plastic strain. With increasing plastic strain during deformation, more retained austenite transforms to martensite and promote the TRIP effect. The low ductility of SMC-6WC samples restricts the TRIP effect pronouncedly, so that the strengthening in strength is also limited.

In order to further reveal the strength-ductility relations of the SMCs prepared via LPBF, the tensile testing for SMCs samples reinforced with different WC content was also conducted and the results are shown in Fig. 14. From the engineering tensile stress-strain curves, one can observe that the tensile strength and elongation of SMC-2WC show synergetic improvements to 1677 ± 125 MPa and 8.5 ± 0.9% respectively, compared to the unreinforced 1.2767L tool steel samples with a tensile strength of 1548 ± 134 MPa and an elongation of 6.2 ± 0.8 %. This confirms that the tensile strength-ductility trade-off is also bypassed in the SMCs prepared in this study. The SMC-4WC samples show a larger tensile strength of 1710 ± 145 MPa but a lower elongation of 5.7 ± 0.6% compared to the SMC-2WC samples. The improvement in tensile strength of SMC-4WC derives from the formation of more $(Fe, W)_6C$ carbides along the cell boundaries which strengthen the composite material effectively. The pronounced deterioration of the

Journal Pre-proof

ductility is due to the presence of microcracks in the SMC-4WC samples. Generally, the tensile property of SMCs is more sensitive to cracks than the compressive property, because the effect of cracks propagation is much pronounced in tension. Therefore, metallurgical defects, including pores and cracks, accelerate the fracture of SMCs samples when subjected to a tensile overload, thus the SMC-6WC samples exhibit a limited tensile property with a tensile strength of 1571 ± 153 MPa and elongation of 3.9 ± 0.8%.

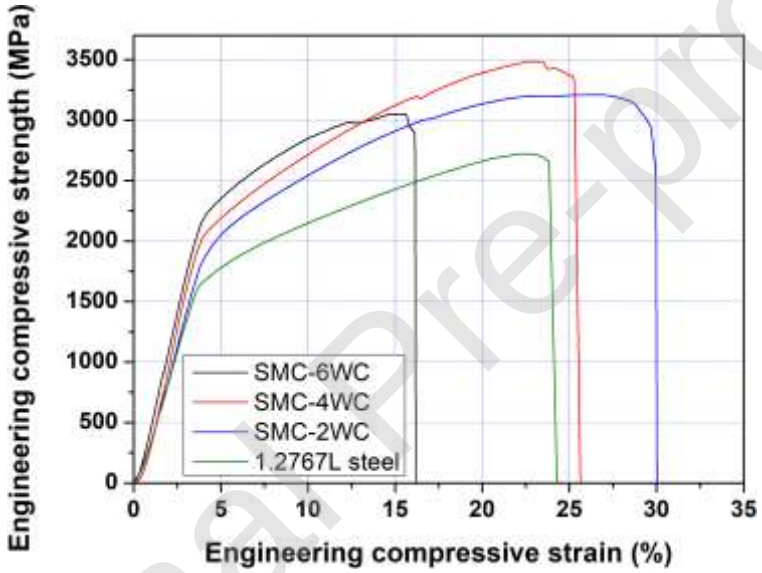

Fig. 11 Representative engineering compressive stress-strain curves of the LPBF-fabricated 1.2767L tool steel and composite samples reinforced with different content of WC.

Journal Pre-proof

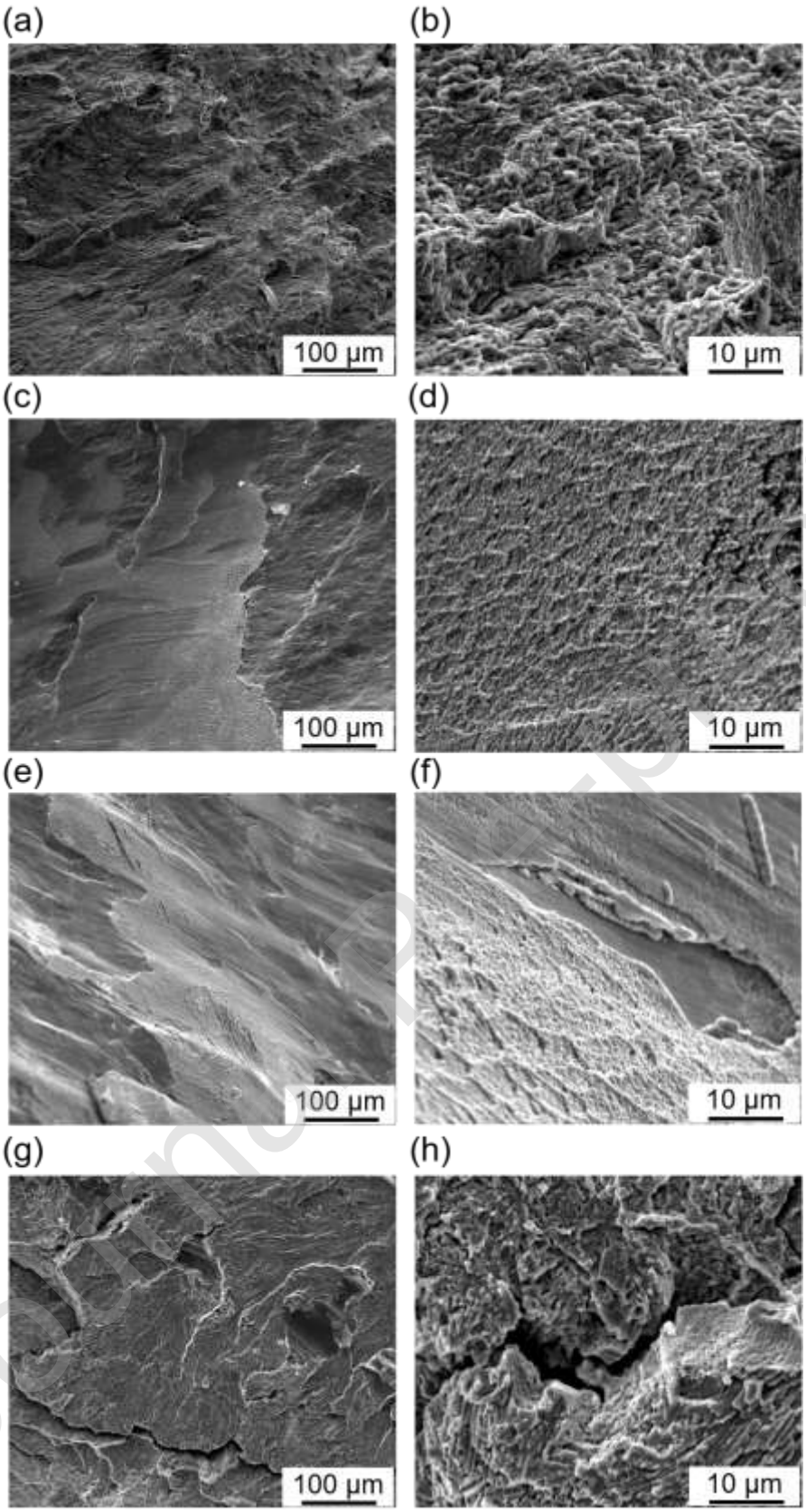

Fig. 12 Typical SEM images taken from the fracture surfaces of LPBF-fabricated 1.2767L tool steel samples (a)-(b) and composite specimens reinforced with (c)-(d) 2 wt% WC, (e)-(f) 4 wt% WC and (g)-(h) 6 wt% WC.

Journal Pre-proof

Journal Pre-proof

Journal Pre-proof

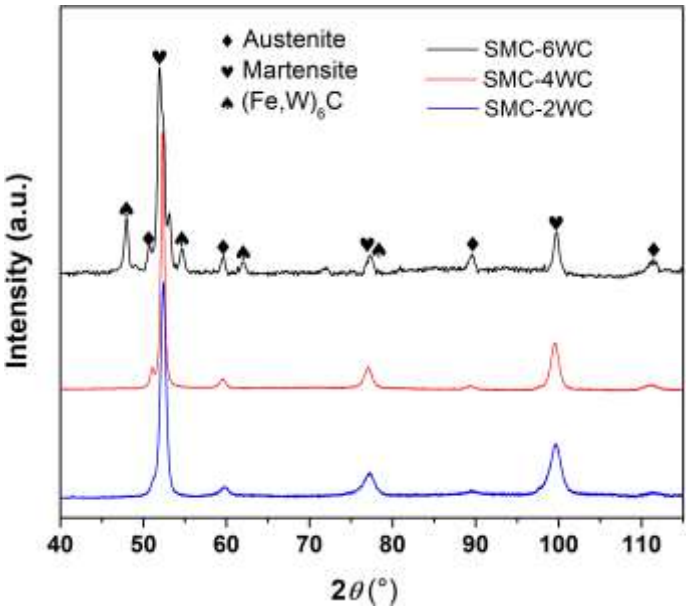

Fig. 13 XRD patterns from the fracture site of LPBF-fabricated SMCs compression samples.

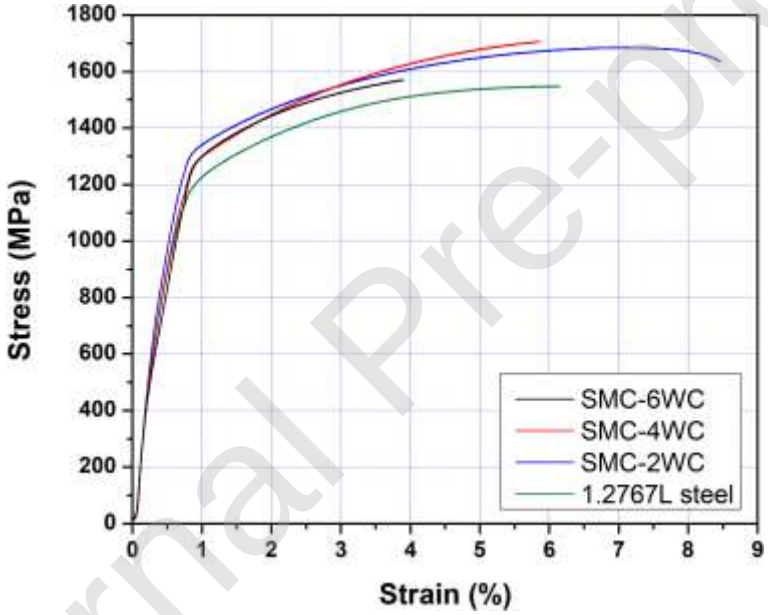

Fig. 14 Representative engineering tensile stress-strain curves of the LPBF-fabricated 1.2767L tool steel and composite samples reinforced with different content of WC.

4. Conclusions

(1) The addition of WC to the tool steel (1.2767L) increase the difficulty of processing fully dense LPFB-fabricated parts. The relative densities of the LPBF-fabricated samples show a linear decrease from 99.8% (LPBF-fabricated 1.2767L steel) to 97.4% as the WC content increases to 6 wt%. The incorporation of WC also significantly affects the phase

Journal Pre-proof

transformation of the iron matrix between austenite and martensite. Especially, C diffusion in the matrix reduces the martensite starting temperature (M_s), distinctly increasing the content of retained austenite from 1.4% to 39.9% with increasing WC content. Additionally, diffused carbon atoms also participate as carbide-type M_6C with the carbide forming elements, such as Fe and W. The $(Fe, W)_6C$ carbide shows a ring-like network morphology with an average thickness from 120 nm to 178 nm and precipitates along the cell boundaries.

(2) The incorporation of WC leads to a significant grain refinement effect within the microstructure of iron-based composites. The formation of $(Fe, W)_6C$ carbides dispersed along sub-grain boundaries inhibit against the growth of austenitic grains which lead to a more refined microstructure compared to the unreinforced steel sample. With addition of 2 wt% WC, the martensite laths become much smaller and narrower with an average size of 0.59 μm in comparison to that without WC (an average size = 2.79 μm). However, a further increase of WC reinforcement up to 4 and to 6 wt% results in the formation of coarser martensite laths with a size of ~1.10 μm. With a higher WC content incorporated in the SMCs, more C atoms segregate along the sub-grain boundaries of the parent austenite and reduce the self-diffusion activation energy of the Fe atom. The decreased self-diffusion activation energy of Fe atoms facilitates the formation and migration of vacancies, resulting in coarser-grained parent austenite and martensite lath.

(3) The formation of the $(Fe, W)_6C$ carbidic phase greatly affects the crystal misorientation of grains of the LPBF-fabricated composites. The martensite laths are always oriented with respect to one of the adjacent lattices of these $(Fe, W)_6C$ carbides

Journal Pre-proof

according to a certain orientation relationship. Thus, the overall crystallographic micro-texture of martensite shows a consistently decreasing trend (the exp. $intensity_{max}$ decreases from 4.2 to 2.0) with increasing WC content. The increase of WC content significantly entails a more isotropic microstructure of the LPBF-manufactured composites.

(4) With the addition of 2 wt% WC, the composites show a synergetic improvement in compressive property with strength of ~3210 MPa and fracture strain up to ~30.2% and tensile property with ultimate strength of ~1677 MPa and elongation of ~8.5% compared to the unreinforced steel parts. The fabricated composites bypass the traditional strength-ductility trade-off dilemma. The combined effects of transformation-induced plasticity (TRIP) effect, grain refinement, formation of non-equilibrium grain boundaries, and precipitation of nano-scaled $(Fe, W)_6C$ carbides are believed to contribute to the strengthening effect of SMCs reinforced with WC.

Credit Author Statement

Hongyu chen: Methodology, Investigation, Data curation, Visualization, Writing-Original draft preparation. **Dongdong Gu:** Conceptualization, Methodology, Validation, Writing - Review & Editing, Supervision. **Tiwen Lu:** Investigation, Data curation**. Liang Deng:** Investigation, Data curation. **Hongmei Zhang:** Investigation, Data curation**. Lixia Xi:** Validation. **Uta Kühn:** Supervision**. Konrad Kosiba:** Validation, Visualization, Writing- Reviewing and Editing**.**

Journal Pre-proof

Conflict of Interest Statement:

This paper mainly focused on synthesizing novel WC-reinforced iron-based composites with excellent mechanical properties by laser additive manufacturing. We declare that we do not have any commercial or associative interest that represents a conflict of interest in connection with the work submitted.

Acknowledgement

We are grateful for the financial support from the National Natural Science Foundation of China (Nos. 51735005), Basic Strengthening Program of Science and Technology (No. 2019-JCJQ-JJ-331), The National Key Research and Development Program "Additive Manufacturing and Laser Manufacturing" (No. 2016YFB1100101), National Natural Science Foundation of China for Creative Research Groups (No. 51921003), and the Priority Academic Program Development of Jiangsu Higher Education Institutions. K.K. thanks the German Science Foundation (DFG) (grant number: KO 5771/1-1) for financial support.

Reference

Almangour, B., Baek, M., Grzesiak, D., Lee, K., 2018. Materials Science & Engineering A Strengthening of stainless steel by titanium carbide addition and grain re fi nement during selective laser melting. Mater. Sci. Eng. A 712, 812–818.

Journal Pre-proof

Journal Pre-proof

https://doi.org/10.1016/j.msea.2017.11.126

AlMangour, B., Grzesiak, D., Yang, J.M., 2017. Scanning strategies for texture and anisotropy tailoring during selective laser melting of TiC/316L stainless steel nanocomposites. J. Alloys Compd. 728, 424–435. https://doi.org/10.1016/j.jallcom.2017.08.022

AlMangour, B., Grzesiak, D., Yang, J.M., 2016. Nanocrystalline TiC-reinforced H13 steel matrix nanocomposites fabricated by selective laser melting. Mater. Des. 96, 150–161. https://doi.org/10.1016/j.matdes.2016.02.022

AlMangour, B., Kim, Y.K., Grzesiak, D., Lee, K.A., 2019. Novel TiB 2 -reinforced 316L stainless steel nanocomposites with excellent room- and high-temperature yield strength developed by additive manufacturing. Compos. Part B Eng. 156, 51–63. https://doi.org/10.1016/j.compositesb.2018.07.050

Boegelein, T., Dryepondt, S.N., Pandey, A., Dawson, K., Tatlock, G.J., 2015. Mechanical response and deformation mechanisms of ferritic oxide dispersion strengthened steel structures produced by selective laser melting. Acta Mater. 87, 201–215. https://doi.org/10.1016/j.actamat.2014.12.047

Bokshteyn, S.Z., 1961. Diffusion and the structure of metals. Met. Sci. Heat Treat. Met. 3, 473–480. https://doi.org/10.1007/BF00814533

Borm, P., Klaessig, F.C., Landry, T.D., Moudgil, B., Pauluhn, J., Thomas, K., Trottier, R., Wood, S., 2006. Research strategies for safety evaluation of nanomaterials, Part V: Role of dissolution in biological fate and effects of nanoscale particles. Toxicol. Sci. 90, 23–32. https://doi.org/10.1093/toxsci/kfj084

Journal Pre-proof

Chawla, K., 2019. Metal Matrix Composites. pp. 199–249. https://doi.org/10.1007/978-3-030-28983-6_6

Chen, H., Gu, D., Dai, D., Xia, M., Ma, C., 2018. A novel approach to direct preparation of complete lath martensite microstructure in tool steel by selective laser melting. Mater. Lett. 227, 128–131. https://doi.org/10.1016/j.matlet.2018.05.042

Chen, H., Gu, D., Deng, L., Lu, T., Kühn, U., Kosiba, K., 2020. Laser additive manufactured high-performance Fe-based composites with unique strengthening structure. J. Mater. Sci. Technol. https://doi.org/https://doi.org/10.1016/j.jmst.2020.04.011

Chen, H., Gu, D., Dai, D., Ma, C., Xia, M., 2017. Microstructure and composition homogeneity, tensile property, and underlying thermal physical mechanism of selective laser melting tool steel parts. Mater. Sci. Eng. A 682, 279–289. https://doi.org/https://doi.org/10.1016/j.msea.2016.11.047

Gao, C., Wang, Z., Xiao, Z., You, D., Wong, K., Akbarzadeh, A.H., 2020. Selective laser melting of TiN nanoparticle-reinforced AlSi10Mg composite: Microstructural, interfacial, and mechanical properties. J. Mater. Process. Technol. 281, 116618. https://doi.org/https://doi.org/10.1016/j.jmatprotec.2020.116618

Gu, D., Ma, J., Chen, H., Lin, K., Xi, L., 2018. Laser additive manufactured WC reinforced Fe-based composites with gradient reinforcement/matrix interface and enhanced performance. Compos. Struct. 192, 387–396. https://doi.org/10.1016/j.compstruct.2018.03.008

Journal Pre-proof

Journal Pre-proof

Gu, D., Chen, H., Dai, D., Ma, C., Zhang, H., Lin, K., Xi, L., Zhao, T., Hong, C., Gasser, A., Poprawe, R., 2020. Carbon Nanotubes Enabled Laser 3D Printing of High-Performance Titanium with Highly Concentrated Reinforcement. iScience 23, 101498. https://doi.org/https://doi.org/10.1016/j.isci.2020.101498

Gu, D., Xia, M., Dai, D., 2019. On the role of powder flow behavior in fluid thermodynamics and laser processability of Ni-based composites by selective laser melting. Int. J. Mach. Tools Manuf. 137, 67–78. https://doi.org/https://doi.org/10.1016/j.ijmachtools.2018.10.006

Hirotsu, Y., Nagakura, S., 1972. Crystal structure and morphology of the carbide precipitated from martensitic high carbon steel during the first stage of tempering. Acta Metall. 20, 645–655. https://doi.org/https://doi.org/10.1016/0001-6160(72)90020-X

Holzweissig, M.J., Taube, A., Brenne, F., Schaper, M., Niendorf, T., 2015. Microstructural Characterization and Mechanical Performance of Hot Work Tool Steel Processed by Selective Laser Melting. Metall. Mater. Trans. B Process Metall. Mater. Process. Sci. 46, 545–549. https://doi.org/10.1007/s11663-014-0267-9

Kalentics, N., Huang, K., Ortega Varela de Seijas, M., Burn, A., Romano, V., Logé, R.E., 2019. Laser shock peening: A promising tool for tailoring metallic microstructures in selective laser melting. J. Mater. Process. Technol. 266, 612–618. https://doi.org/https://doi.org/10.1016/j.jmatprotec.2018.11.024

Li, B., Qian, B., Xu, Y., Liu, Z., Zhang, J., Xuan, F., 2019. Additive manufacturing of

Journal Pre-proof

Journal Pre-proof

ultrafine-grained austenitic stainless steel matrix composite via vanadium carbide reinforcement addition and selective laser melting: Formation mechanism and strengthening effect. Mater. Sci. Eng. A 745, 495–508. https://doi.org/https://doi.org/10.1016/j.msea.2019.01.008

Liu, D., Li, L., Li, F., Chen, Y., 2008. WCp/Fe metal matrix composites produced by laser melt injection. Surf. Coatings Technol. 202, 1771–1777. https://doi.org/10.1016/j.surfcoat.2007.07.053

Liu, G., Zhang, G.J., Jiang, F., Ding, X.D., Sun, Y.J., Sun, J., Ma, E., 2013. Nanostructured high-strength molybdenum alloys with unprecedented tensile ductility. Nat. Mater. 12, 344–350. https://doi.org/10.1038/nmat3544

Pacchioni, G., 2017. 3D printing: May the strength be with you. Nat. Rev. Mater. 2, 17081. https://doi.org/10.1038/natrevmats.2017.81

Pauly, S., Wang, P., Kühn, U., Kosiba, K., 2018. Experimental determination of cooling rates in selectively laser-melted eutectic Al-33Cu. Addit. Manuf. 22, 753–757. https://doi.org/10.1016/j.addma.2018.05.034

Sander, J., Hufenbach, J., Giebeler, L., Wendrock, H., Kühn, U., Eckert, J., 2016. Microstructure and properties of FeCrMoVC tool steel produced by selective laser melting. Mater. Des. 89, 335–341. https://doi.org/10.1016/j.matdes.2015.09.148

Song, C., Wang, H., Sun, Z., Wei, Z., Yu, H., Chen, H., Wang, Y., Lu, J., 2020. Effect of multiphase microstructure on fatigue crack propagation behavior in TRIP-assisted steels. Int. J. Fatigue 133, 105425. https://doi.org/https://elkssl0a75e822c6f3334851117f8769a30e1cportal.i.nuaa.edu.

Journal Pre-proof

Journal Pre-proof

cn:4443/10.1016/j.ijfatigue.2019.105425

Su, Y., Song, R., Wang, T., Cai, H., Wen, J., Guo, K., 2020. Grain size refinement and effect on the tensile properties of a novel low-cost stainless steel. Mater. Lett. 260, 126919. https://doi.org/10.1016/j.matlet.2019.126919

van Bohemen, S.M.C., 2012. Bainite and martensite start temperature calculated with exponential carbon dependence. Mater. Sci. Technol. 28, 487–495. https://doi.org/10.1179/1743284711Y.0000000097

Vasilyev, A.A., Sokolov, S.F., Kolbasnikov, N.G., Sokolov, D.F., 2011. Effect of alloying on the self-diffusion activation energy in γ-iron. Phys. Solid State 53, 2194–2200. https://doi.org/10.1134/S1063783411110308

Wang, J., Li, L., Tao, W., 2016. Crack initiation and propagation behavior of WC particles reinforced Fe-based metal matrix composite produced by laser melting deposition. Opt. Laser Technol. 82, 170–182. https://doi.org/10.1016/j.optlastec.2016.03.008

Wang, Y.M., Voisin, T., McKeown, J.T., Ye, J., Calta, N.P., Li, Z., Zeng, Z., Zhang, Y., Chen, W., Roehling, T.T., Ott, R.T., Santala, M.K., Depond, P.J., Matthews, M.J., Hamza, A. V., Zhu, T., 2018. Additively manufactured hierarchical stainless steels with high strength and ductility. Nat. Mater. 17, 63–70. https://doi.org/10.1038/NMAT5021

Yan, X., Huang, C., Chen, C., Bolot, R., Dembinski, L., 2019. Surface & Coatings Technology Additive manufacturing of WC reinforced maraging steel 300 composites by cold spraying and selective laser melting. Surf. Coat. Technol. 371,

Journal Pre-proof

Journal Pre-proof

161–171. https://doi.org/10.1016/j.surfcoat.2018.03.072

Zhang, H., Gu, D., Ma, C., Guo, M., Yang, J., Wang, R., 2019. Effect of post heat treatment on microstructure and mechanical properties of Ni-based composites by selective laser melting. Mater. Sci. Eng. A 765, 138294. https://doi.org/https://doi.org/10.1016/j.msea.2019.138294

Zhang, M., Chen, H., Wang, Y., Wang, S., Li, R., Li, S., Wang, Y.D., 2019. Deformation-induced martensitic transformation kinetics and correlative micromechanical behavior of medium-Mn transformation-induced plasticity steel. J. Mater. Sci. Technol. 35, 1779–1786. https://doi.org/10.1016/j.jmst.2019.04.007

Zhang, Z., Chen, D.L., 2006. Consideration of Orowan strengthening effect in particulate-reinforced metal matrix nanocomposites: A model for predicting their yield strength. Scr. Mater. 54, 1321–1326. https://doi.org/https://doi.org/10.1016/j.scriptamat.2005.12.017

Journal Pre-proof

Journal Pre-proof

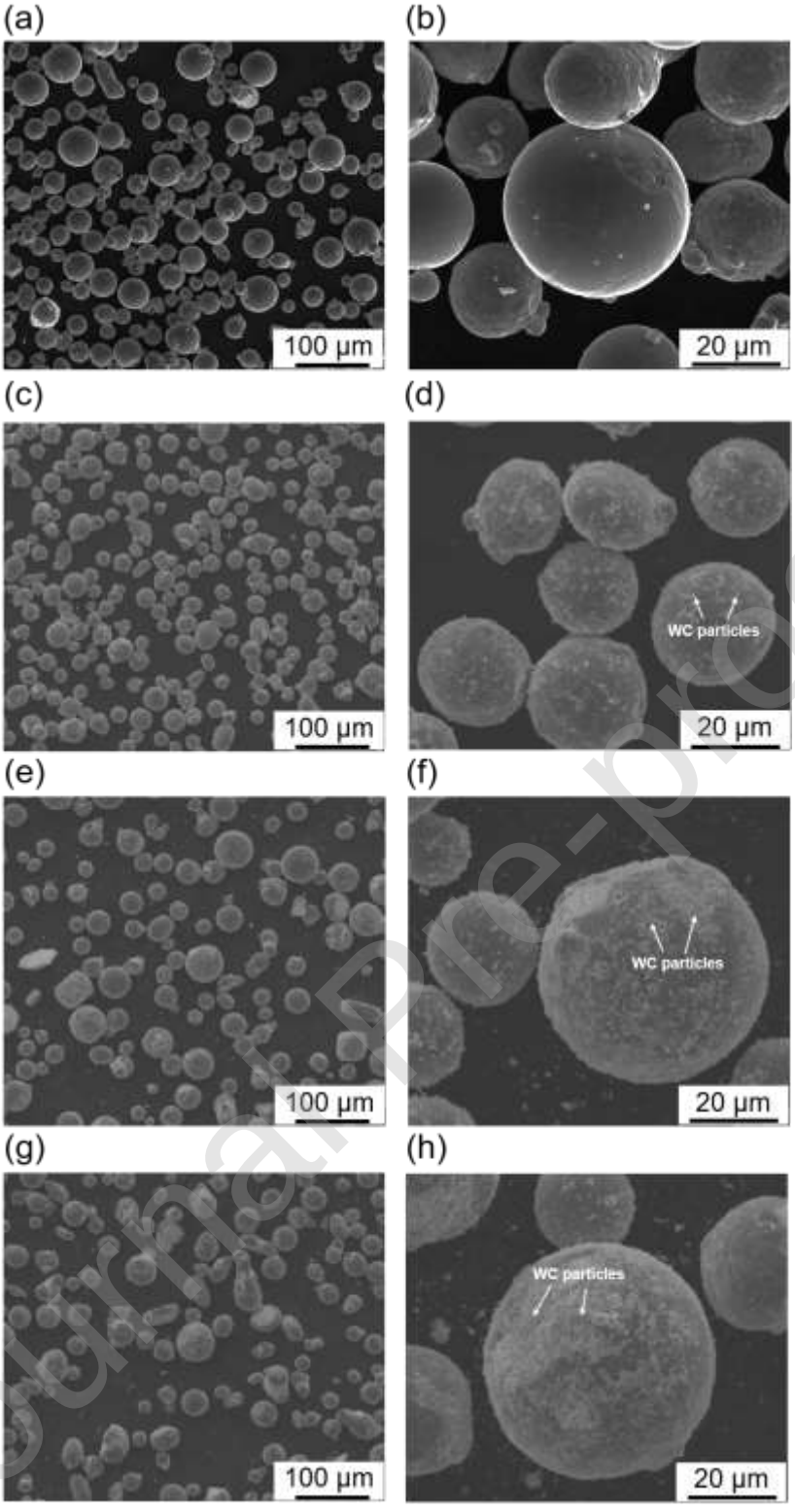

Fig. 1 Scanning electron microscope (SEM) images show typical morphologies of the tool steel powder (a) and as-prepared composite powder containing different weight fraction of WC particles: (c)-(d) 2 wt% WC; (e)-(f) 4 wt% WC; (g)-(h) 6 wt% WC.

Journal Pre-proof

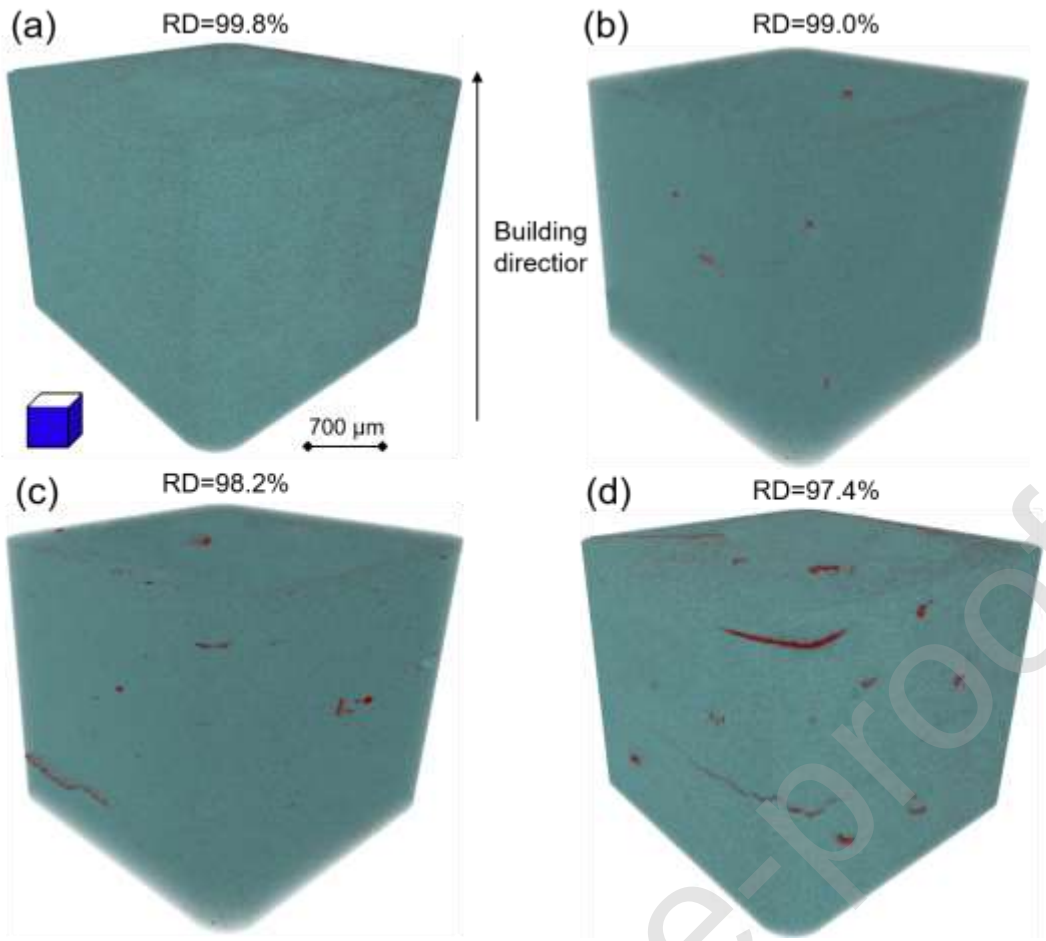

Fig. 2 The µ-CTs reveal the distribution of pores within LPBF-fabricated 1.2767L tool steel (a) and composite samples reinforced with (b) 2 wt% WC, (c) 4 wt% WC and (d) 6 wt% WC.

Journal Pre-proof

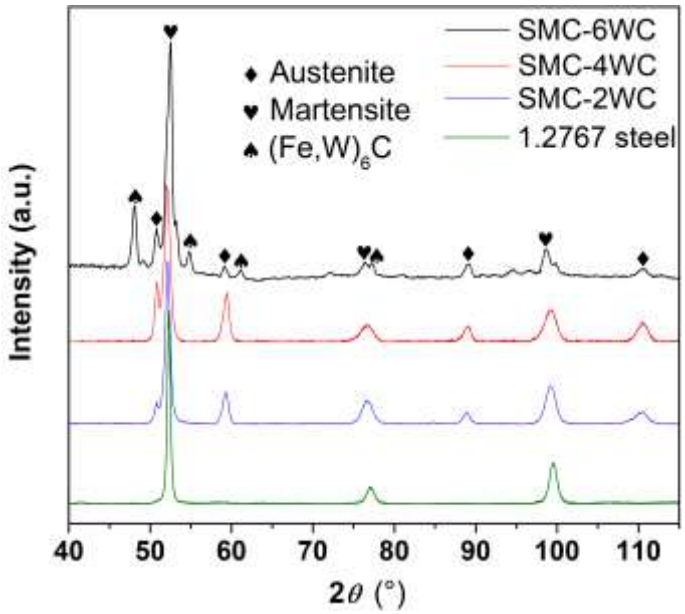

Fig. 3 XRD patterns of LPBF-fabricated tool steel and composite samples reinforced with different content of WC.

Journal Pre-proof

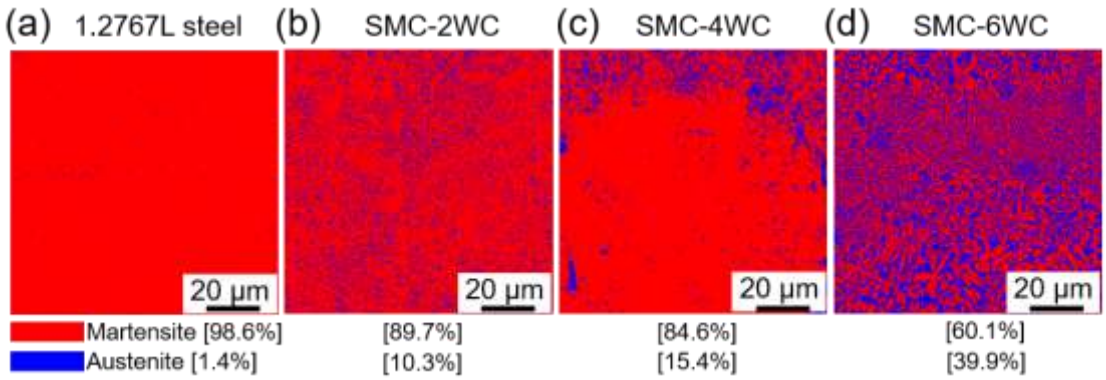

Fig. 4 EBSD analysis shows the phase map and volume fraction of austenite and martensite within LPBF-fabricated 1.2767L tool steel (a) and composite samples reinforced with (b) 2 wt% WC, (c) 4 wt% WC and (d) 6 wt% WC.

Journal Pre-proof

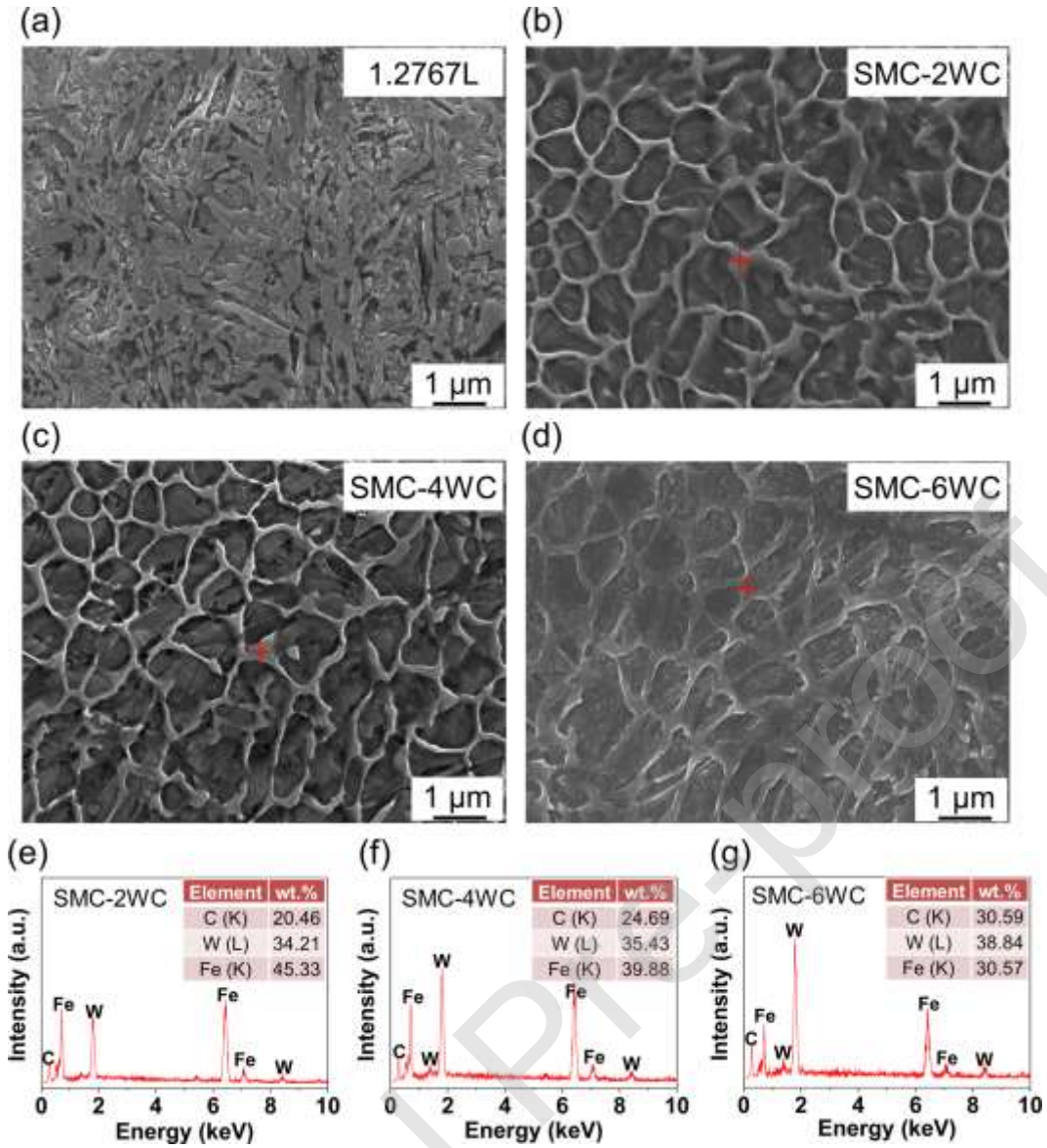

Fig. 5 SEM images highlight the martensite microstructure of 1.2767L tool steel (a) and cellular microstructure of the composite reinforced with (b) 2 wt% WC, (c) 4 wt% WC and (d) 6 wt% WC. (e)-(f) depict the respective EDS analysis carried out at the locations indicated with the red crosses in (b)-(d).

Journal Pre-proof

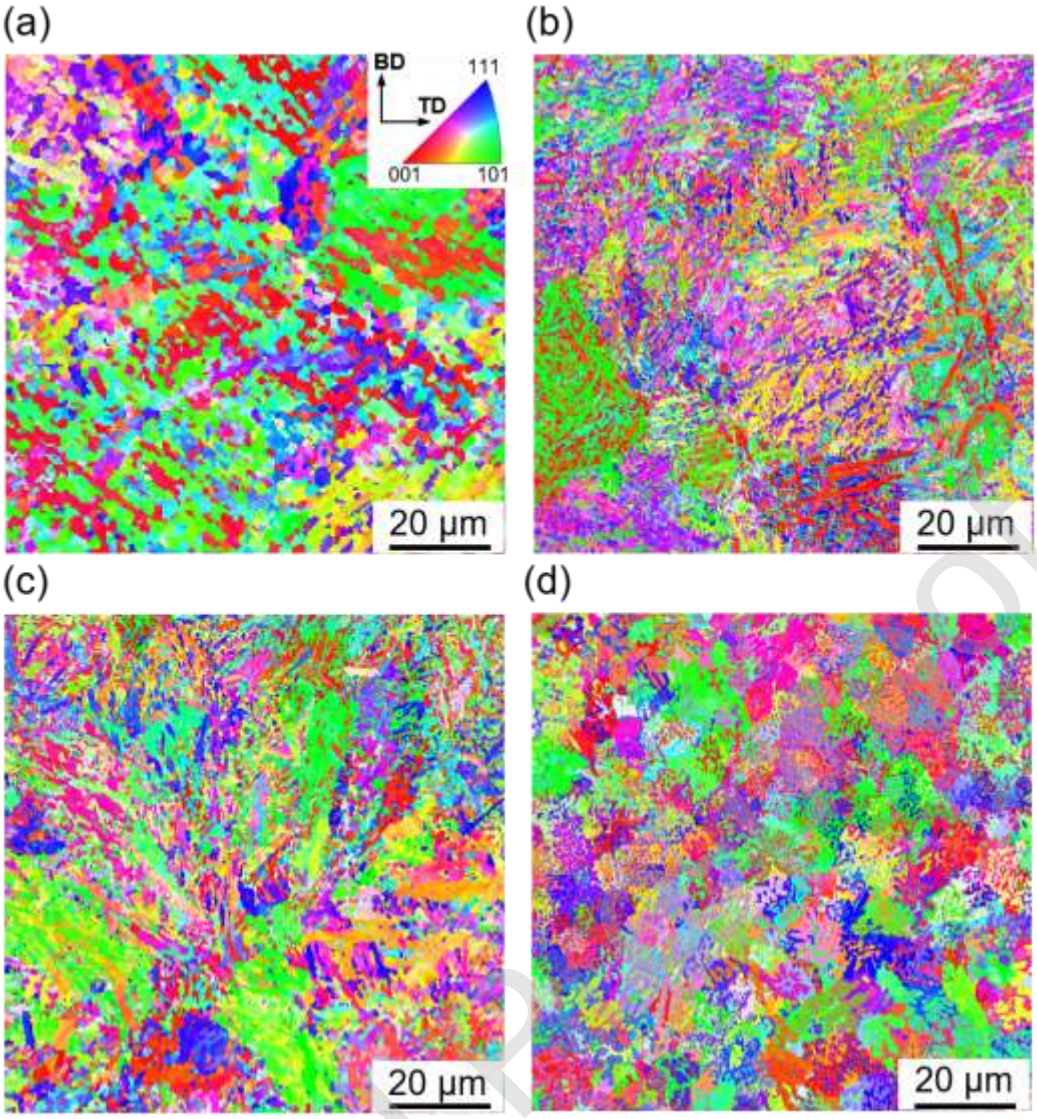

Fig. 6 Inverse Pole Figure (IPF) mapping of LPBF-fabricated 1.2767L tool steel (a) and iron-based matrix within composite samples reinforced with (b) 2 wt% WC, (c) 4 wt% WC and (d) 6 wt% WC.

Journal Pre-proof

Journal Pre-proof

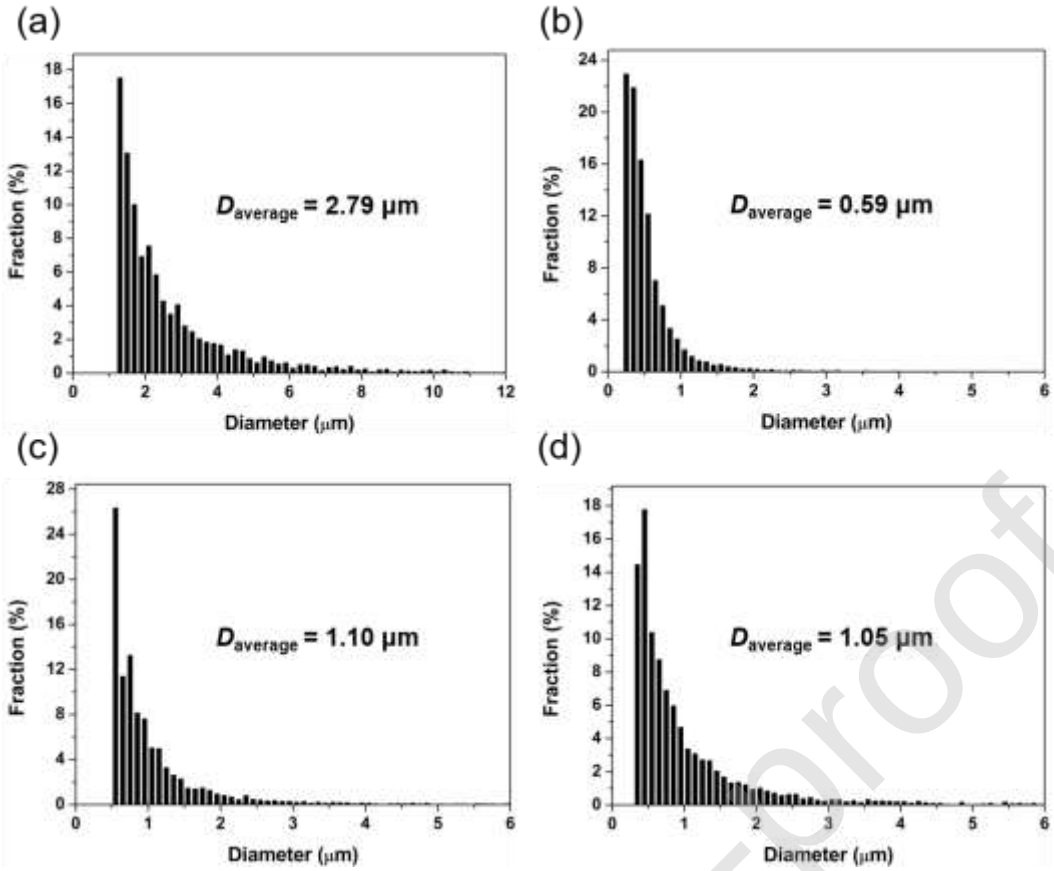

Fig. 7 EBSD analysis shows the grain size distribution for LPBF-fabricated 1.2767L tool steel (a) and iron-based matrix in composite samples reinforced with (b) 2 wt% WC, (c) 4 wt% WC and (d) 6 wt% WC.

Journal Pre-proof

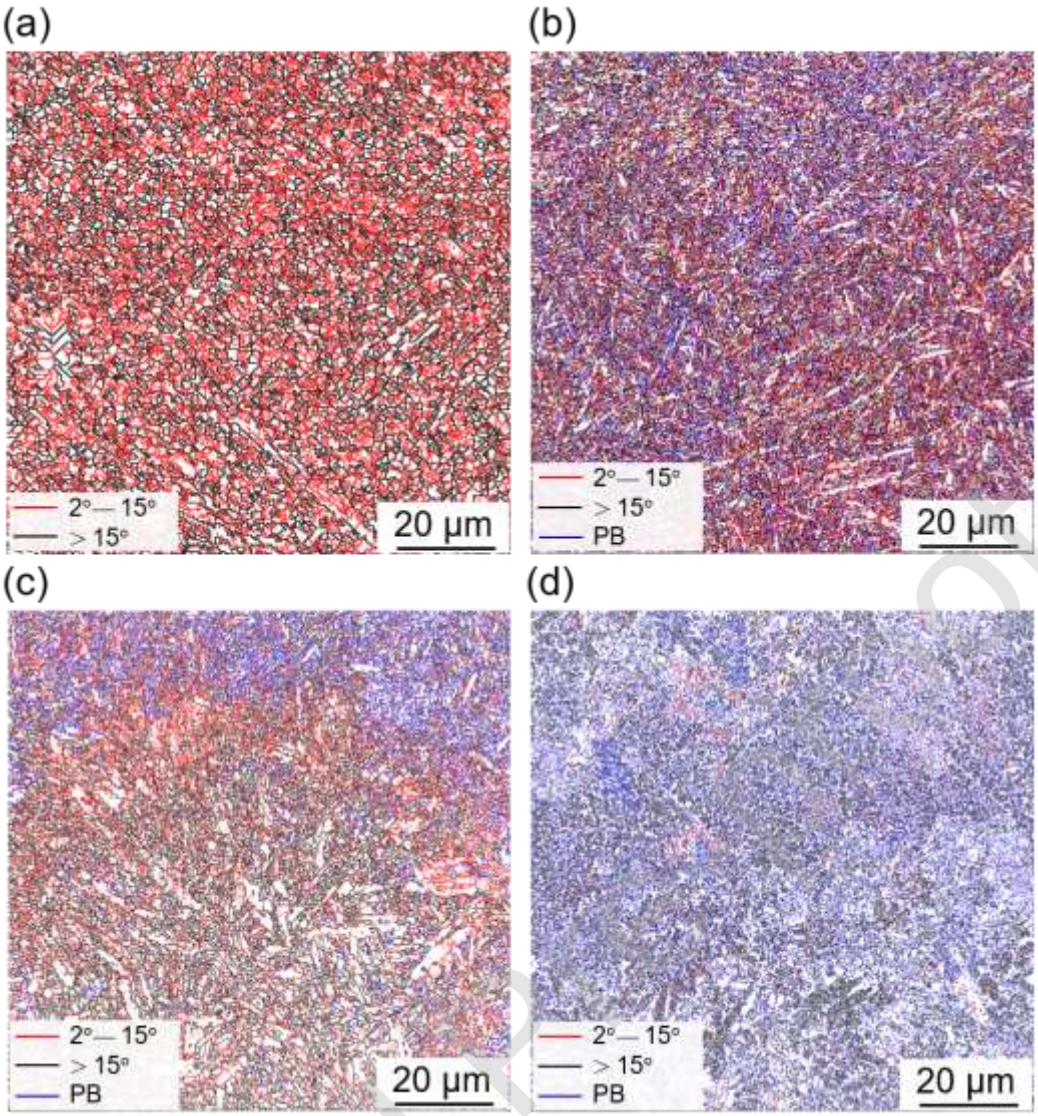

Fig. 8 Grain boundary distribution map for LPBF-fabricated 1.2767L tool steel (a) and iron-based matrix in composite samples reinforced with (b) 2 wt% WC, (c) 4 wt% WC and (d) 6 wt% WC. Thereby, HAGBs are defined with a misorientation angle of 15°-66.8° and LAGBs are defined with a misorientation angle of 2°-15°.

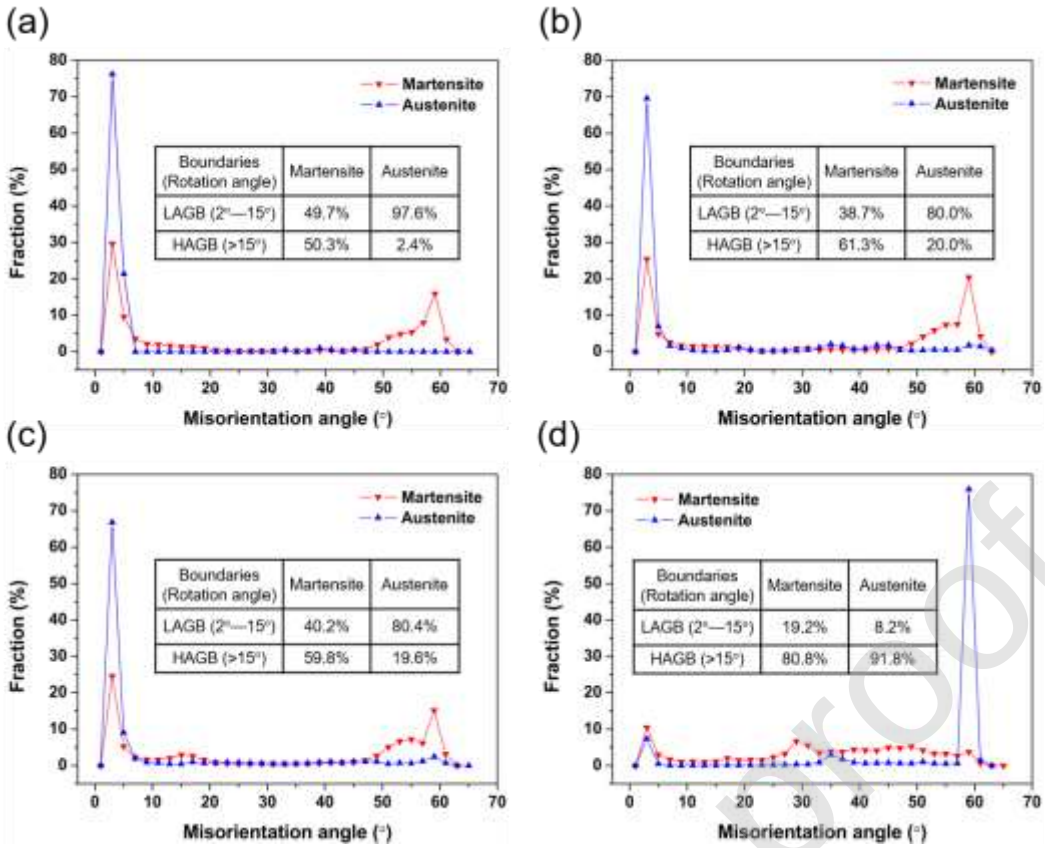

Fig. 9 Misorientation angle distribution for martensite and austenite in LPBF-fabricated 1.2767L tool steel (a) and composite samples reinforced with (b) 2 wt% WC, (c) 4 wt% WC and (d) 6 wt% WC.

Journal Pre-proof

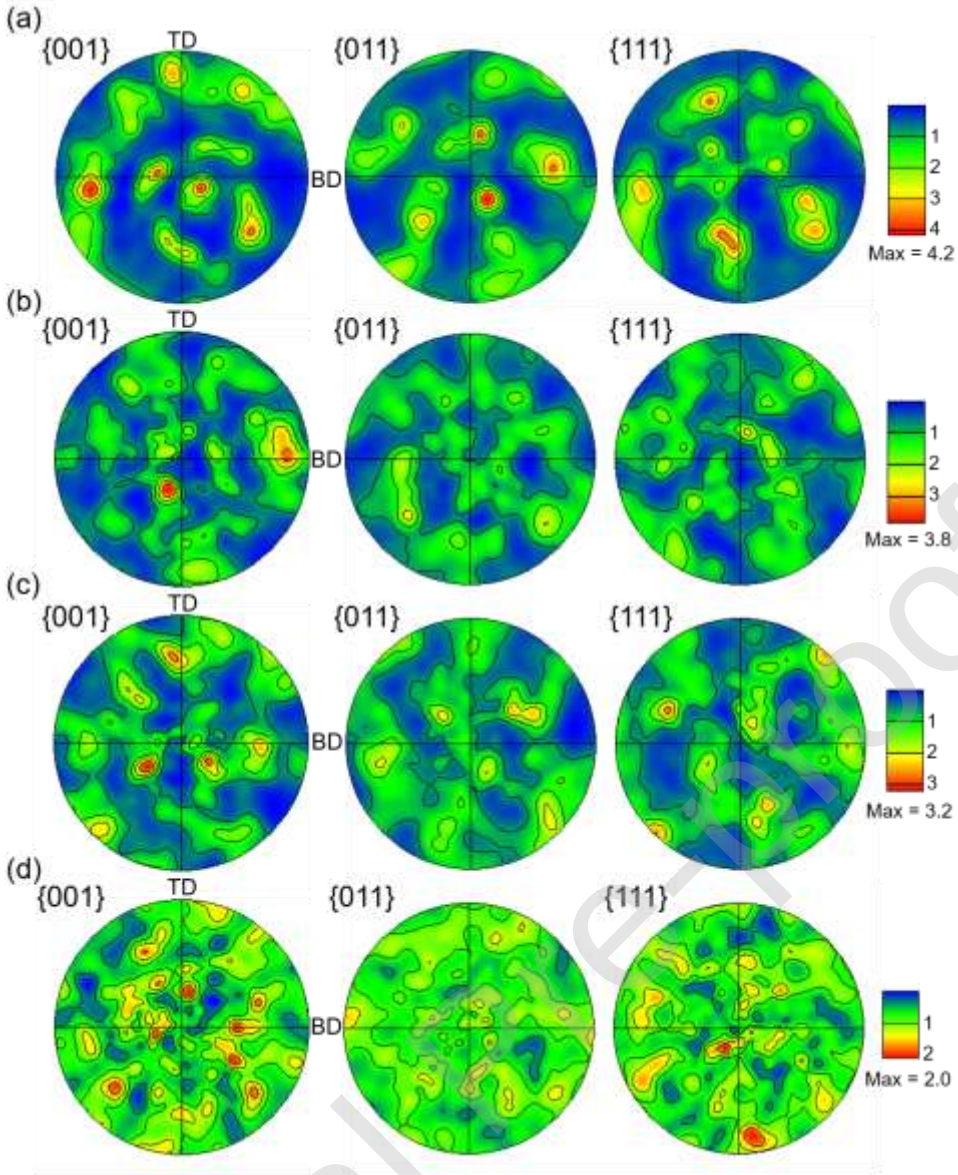

Fig. 10 Pole figure (PF) plots quantify the micro-texture intensities of martensite along the three crystallographic direction-families <001>, <101> and <111> with respect to the surface of the LPBF-fabricated 1.2767L tool steel (a) and composite samples reinforced with (b) 2 wt% WC, (c) 4 wt% WC and (d) 6 wt% WC.

Journal Pre-proof

Journal Pre-proof

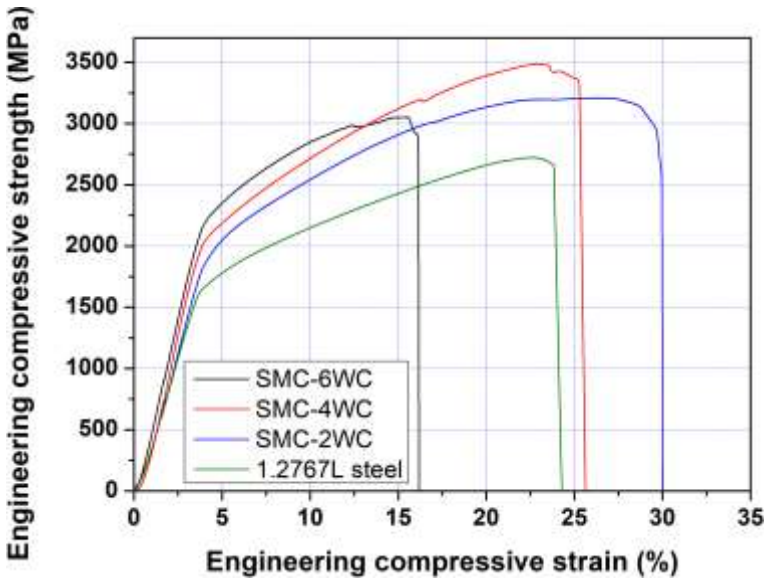

Fig. 11 Representative engineering compressive stress-strain curves of the LPBF-fabricated 1.2767L tool steel and composite samples reinforced with different content of WC.

Journal Pre-proof

Journal Pre-proof

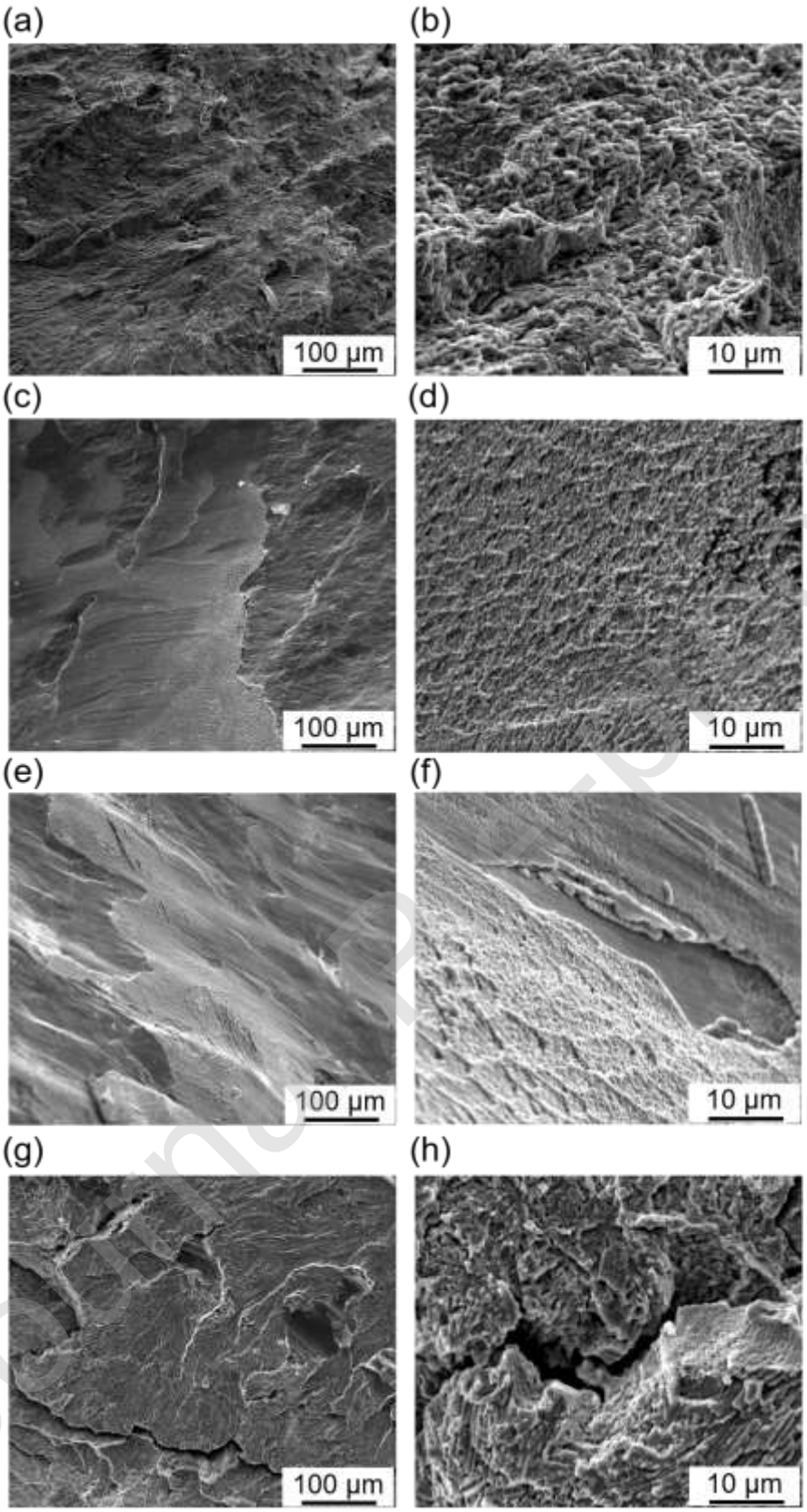

Fig. 12 Typical SEM images taken from the fracture surfaces of LPBF-fabricated 1.2767L tool steel samples (a)-(b) and composite specimens reinforced with (c)-(d) 2 wt% WC, (e)-(f) 4 wt% WC and (g)-(h) 6 wt% WC.

Journal Pre-proof

Journal Pre-proof

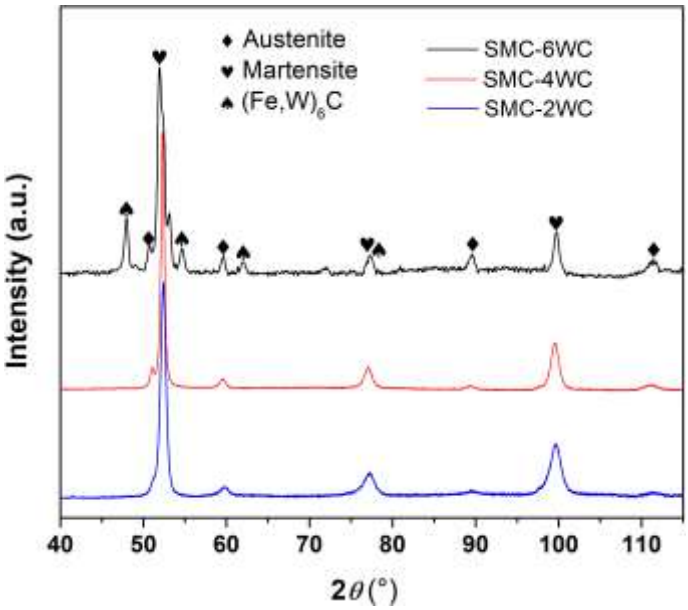

Fig. 13 XRD patterns from the fracture site of LPBF-fabricated SMCs compression samples.

Journal Pre-proof

Journal Pre-proof

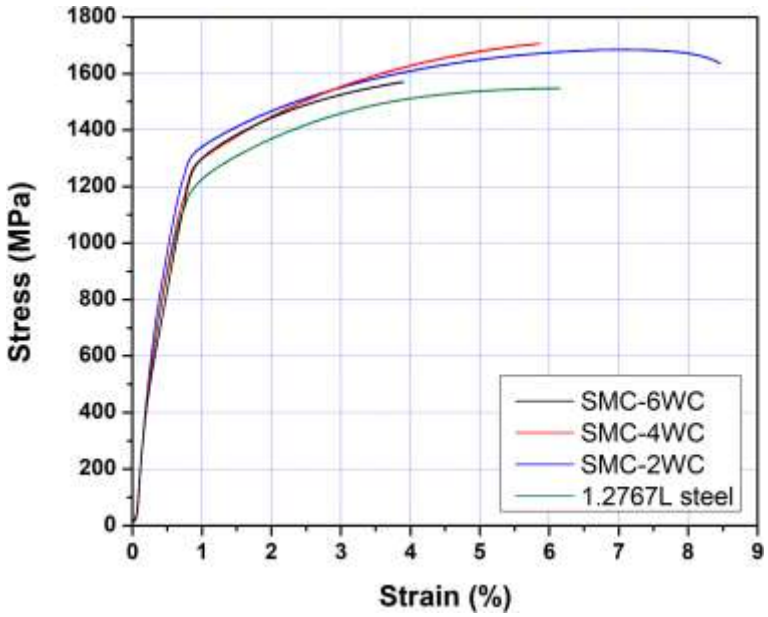

Fig. 14 Representative engineering tensile stress-strain curves of the LPBF-fabricated 1.2767L tool steel and composite samples reinforced with different content of WC.

Journal Pre-proof